

# Integrative single-cell metabolomics and phenotypic profiling reveals metabolic heterogeneity of cellular oxidation and senescence

Received: 18 April 2024

Accepted: 10 March 2025

Published online: 20 March 2025



Ziyi Wang<sup>1</sup>, Siyuan Ge<sup>1</sup>, Tiepeng Liao<sup>1</sup> , Man Yuan<sup>1</sup>, Wenwei Qian<sup>1</sup>, Qi Chen<sup>1</sup>, Wei Liang<sup>1</sup>, Xiawei Cheng<sup>2</sup> , Qinghua Zhou<sup>3</sup> , Zhenyu Ju<sup>3</sup> , Hongying Zhu<sup>1,4,5,6</sup>  & Wei Xiong<sup>1,4,5,6</sup> 

Emerging evidence has unveiled heterogeneity in phenotypic and transcriptional alterations at the single-cell level during oxidative stress and senescence. Despite the pivotal roles of cellular metabolism, a comprehensive elucidation of metabolomic heterogeneity in cells and its connection with cellular oxidative and senescent status remains elusive. By integrating single-cell live imaging with mass spectrometry (SCLIMS), we establish a cross-modality technique capturing both metabolome and oxidative level in individual cells. The SCLIMS demonstrates substantial metabolomic heterogeneity among cells with diverse oxidative levels. Furthermore, the single-cell metabolome predicted heterogeneous states of cells. Remarkably, the pre-existing metabolomic heterogeneity determines the divergent cellular fate upon oxidative insult. Supplementation of key metabolites screened by SCLIMS resulted in a reduction in cellular oxidative levels and an extension of *C. elegans* lifespan. Altogether, SCLIMS represents a potent tool for integrative metabolomics and phenotypic profiling at the single-cell level, offering innovative approaches to investigate metabolic heterogeneity in cellular processes.

With the advancements in single-cell analysis techniques, the heterogeneity of single-cell genetics, proteomics, and metabolomics has captivated the attention of scientists for decades. The phenotypic and transcriptional heterogeneity of individual cells has been extensively elucidated in diverse biological processes, encompassing development, cancer, and aging. For instance, through the lens of single-cell

transcriptomic studies, developmental trajectories are meticulously unraveled, unveiling the exquisite tapestry of single-cell heterogeneity and sub-populations during embryonic development<sup>1,2</sup>. The genetic and epigenetic heterogeneity exhibited by cancer cells<sup>3</sup> poses significant challenges in the field of cancer therapy<sup>4</sup>. Delving into the single-cell heterogeneity of these cells illuminates promising avenues

<sup>1</sup>Department of Neurology, The First Affiliated Hospital of USTC, Division of Life Sciences and Medicine, University of Science and Technology of China, 230001 Hefei, China. <sup>2</sup>School of Pharmacy, Optogenetics & Synthetic Biology Interdisciplinary Research Center, East China University of Science and Technology, 200237 Shanghai, China. <sup>3</sup>Key Laboratory of Regenerative Medicine of Ministry of Education, Institute of Aging and Regenerative Medicine, Department of Developmental & Regenerative Medicine, College of Life Science and Technology, Jinan University, 510632 Guangzhou, Guangdong, China. <sup>4</sup>Anhui Province Key Laboratory of Biomedical Imaging and Intelligent Processing, Institute of Artificial Intelligence, Hefei Comprehensive National Science Center, 230088 Hefei, China. <sup>5</sup>CAS Key Laboratory of Brain Function and Disease, 230026 Hefei, China. <sup>6</sup>Anhui Province Key Laboratory of Biomedical Aging Research, 230026 Hefei, China. ✉e-mail: [zhuhy62@ustc.edu.cn](mailto:zhuhy62@ustc.edu.cn); [wxiong@ustc.edu.cn](mailto:wxiong@ustc.edu.cn)

for therapeutic targets and strategies<sup>5,6</sup>. It has been reported that geriatric organs are mosaics of cells with varying ages, thereby highlighting the remarkable heterogeneity exhibited by individual cells during the process of aging<sup>7</sup>. Another study uncovers the heterogeneity of transcriptional landscape in aged ovaries where genes undergo specific changes during aging that are exclusive to different oocyte subtypes<sup>8</sup>. In essence, comprehending cellular heterogeneity is paramount in unraveling the intricate cellular mechanisms that underlie biological processes, including development, aging, and diseases.

A groundbreaking advancement in single-cell research lies in the seamless integration of multiple features or functions within individual cells, known as cross-modality analysis. This includes integrating single-cell omics with cellular function or phenotype, resulting in a truly remarkable and sophisticated approach<sup>9,10</sup>. For instance, with the Patch-seq technique, single-cell transcriptome and electric activities are combined, linking transcriptome to cellular function<sup>11</sup>. In a study investigating the exocytosis and excretion function of pancreatic  $\beta$ -cells in diabetes, the Patch-seq technology was employed to establish a connection between  $\beta$ -cell functionality, as represented by electrical activities, and gene expression profiles. This innovative approach successfully identified genes that are closely associated with  $\beta$ -cell dysfunction<sup>11</sup>. Another study on extracellular vesicles (EV) links lipidomics and proteomic with EV membrane function and crosstalk of discrete tissues in different stages of COVID-19 infection<sup>12</sup>. The integrative analysis of metabolism and transcriptome reveals a rare subpopulation of hyperactive T cells and subtypes of monocyte which links to disease severity in COVID-19, suggesting an association between multi-omics and immune cell functionality<sup>13</sup>. The combination of single-cell RNAseq and fluorescence-activated cell sorting (FACS) illustrates the relation between gene expression and stem cell function represented by specific surface markers, discovering key molecules associated with self-renewal in stem cells<sup>14</sup>. Thus, the cross-modality analysis enables a more comprehensive view of single-cell omics and a deeper understanding of cellular function, shedding light on mechanisms underlying complicated biological processes.

Metabolism serves as both a reflection and regulator of cellular function<sup>15</sup>. Currently, most metabolomics research remains confined to homogenate-level analysis involving the preparation of samples using bulk tissue or cell suspension. Consequently, the enigmatic metabolic heterogeneity exhibited by cells during biological processes and the underlying mechanisms at the single-cell level remain shrouded in ambiguity. Recently, our laboratory and others have pioneered the development of cutting-edge single-cell mass spectrometry techniques, enabling us to unveil the intricate metabolic heterogeneity at an unprecedented resolution<sup>16–18</sup>. These new techniques mainly focused on the interpretation of the metabolome without the phenotype of single cells, omitting cross-modality features important for the better understanding of cellular metabolism and function. However, the integration of metabolic heterogeneity with phenotypic heterogeneity, such as distinct levels of oxidative or senescent states within individual cells, remains a formidable technical challenge.

In the present study, we employ a combination of single-cell mass spectrometry (SCMS) and live-cell imaging techniques to simultaneously capture the metabolomic features and cellular identities of individual cells, thereby establishing a link between the metabolome and cellular status at a single-cell resolution. By utilizing this approach, we design our study using a cellular model of oxidative stress-induced senescence, establishing the correlation between single-cell metabolome and their oxidative or senescent status. This technique unlocks possibilities in the realm of cross-modality analysis, integrating single-cell metabolome with fluorescent labeling techniques, thereby paving the way for innovative discoveries at the single-cell level.

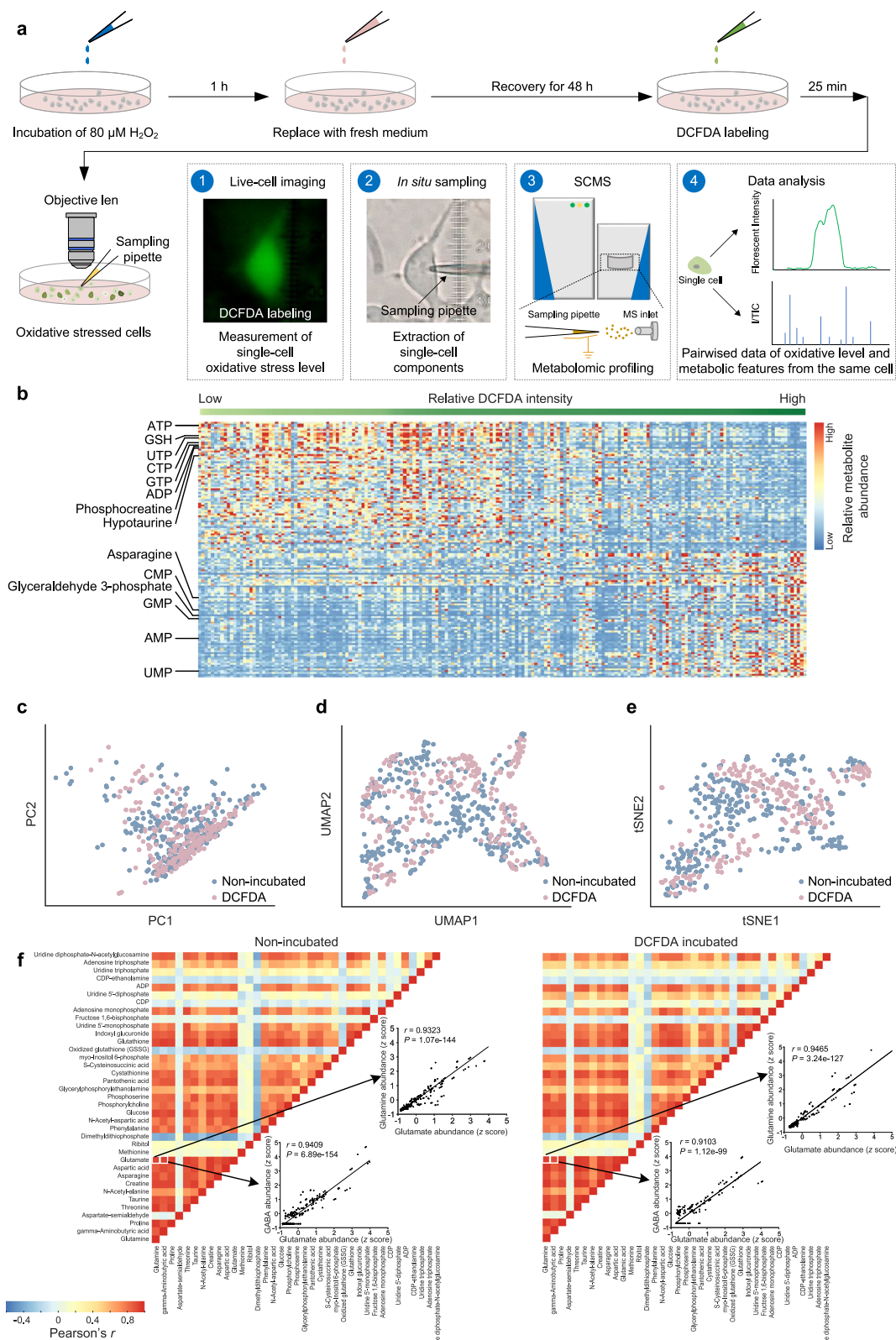
## Results

### Integration of live-cell imaging and single-cell mass spectrometry

To simultaneously capture the metabolome and phenotypic features of a single cell, we combined single-cell live imaging with mass spectrometry technique<sup>17,18</sup> (SCLIMS) and setup a cross-modality analysis platform. We employed a cellular oxidative stress (OS) model<sup>19–24</sup> which can be readily induced and labeled with dichlorodihydrofluorescein diacetate (DCFDA), a widely utilized live-cell probe for the detection of cellular OS<sup>8,25,26</sup>. Briefly, HEK293T cells were incubated with H<sub>2</sub>O<sub>2</sub> in culture medium at a final concentration of 80  $\mu$ M for 1 h, and the medium was then replaced by fresh medium. The cells were allowed to recover for 48 h prior to subsequent testing. Cellular viability remained uncompromised in the model and was deemed suitable for SCMS analysis (Supplementary Fig. 1a). The OS level was evaluated through DCFDA staining<sup>8,25,26</sup> (Supplementary Fig. 1b, c). Initially, the cells were incubated with DCFDA for a duration of 25 min and then imaged using a microscope. Subsequently, cellular sampling was performed via patch clamp technique utilizing micro-pipettes, followed by SCMS analysis. Finally, the fluorescent intensity was calculated and paired with metabolomic features in single cells, yielding a pairwise dataset of metabolome and oxidative levels (Fig. 1a).

In  $m/z$  ranging from 67 to 1000, a total of more than 500 ion signals, with signal-to-noise ratio greater than 3 (refs. 27,28) and detected at a frequency greater than 20% in all single cells were used in subsequent analysis. Among these signals, 162 matched annotations in the HMDB database through MS spectra. The annotated metabolites underwent further scrutiny via MS/MS, resulting in confirmation of 83 metabolites that were subsequently employed for pathway enrichment analysis (Supplementary Data File 1). Fluorescent intensities of sampled cells were calculated and matched to every single cell. The heatmap illustrated the metabolite abundance and corresponding DCFDA intensity in single cells, showing the gradual alteration of metabolism as DCFDA intensity differs (Fig. 1b). A variety of metabolites, exhibiting diverse changes in response to DCFDA intensification, including glutathione (GSH), phosphocreatine, hypotaurine and adenosine triphosphate (ATP), were unearthed, suggesting a profound impact of OS on cellular metabolism.

To rule out the possibility that DCFDA incubation may disturb cellular metabolism, we analyzed the metabolome of the cells treated with or without DCFDA by using analysis methods including Principal component analysis (PCA), uniform manifold approximation and projection (UMAP), and t-distributed stochastic neighbor embedding (t-SNE). As a result, no significant difference in cellular metabolome between DCFDA incubated and non-incubated cells was observed (Fig. 1c–e). Consistently, the abundance of 31 common metabolites including GSH, ATP, adenosine diphosphate (ADP), glutamate, glutamine, creatine, oxidized glutathione (GSSG), phosphorylcholine, and phosphoserine were almost identical in DCFDA incubated and non-incubated cells (Supplementary Fig. 1d). We further performed a correlation analysis of metabolites in both DCFDA incubated and non-incubated cells, revealing the similarity in the correlations among metabolites. As shown in the heatmap, the correlation coefficients between metabolites remain virtually indistinguishable in both DCFDA incubated and non-incubated cells (Fig. 1f), suggesting that the metabolic landscape was not significantly altered by DCFDA incubation. For instance, the correlation and conversion of metabolites in the classical glutamine-glutamate-GABA metabolic pathway remained unaffected by the incubation of DCFDA, as evidenced by a robust association between glutamate and GABA, as well as between glutamine and glutamate, observed in both DCFDA-incubated and non-incubated cells. The difference of correlation coefficients ( $r$ ) between non-incubated and DCFDA incubated cells



was calculated and visually represented using a heatmap (Supplementary Fig. 1e), illustrating minimal divergence in the correlations of metabolites within the non-incubated and DCFDA incubated cells. Altogether, the cross-modality analysis platform successfully integrated single-cell metabolome and cellular phenotype with high stability and reliability, while preserving cellular viability and metabolism.

### The SCLIMS reveals correlation between cellular metabolism and oxidative levels

The Multi-modal properties of SCLIMS facilitate its capacity to explore the link between cellular metabolism and their OS levels, by means of conducting correlation analysis between single-cell metabolomics data and DCFDA intensity in each cell (Fig. 2a). The metabolomics data was confirmed with no obvious batch effect by PCA and HCA

**Fig. 1 | The cross-modality analysis platform integrating single-cell metabolome and cellular phenotype.** **a** A workflow and experimental setup of the cross-modality analysis. Cells were first labeled with DCFDA and photographed with a fluorescent microscope, followed by sampling and single-cell MS analysis. The oxidative levels were reflected by DCFDA fluorescent intensity and the metabolic information was acquired by SCMS. **b** Heatmap showing relative abundance of representative metabolites corresponding to single-cell DCFDA intensity. DCFDA intensity was indicated by color: dark green, relative high intensity; light green, relative low intensity. Metabolite abundance was represented by color: red, relative

high abundance; blue, relative low abundance. **c–e** PCA score plot (**c**), UMAP analysis (**d**), and tSNE analysis (**e**) showing no significant difference in metabolome of DCFDA incubated ( $n = 257$ , pink) and non-incubated cells ( $n = 325$ , blue). **f** Correlation heatmap illustrating Pearson's correlation coefficient ( $r$ ) between metabolites in non-incubated (left,  $n = 325$ ) and DCFDA incubated (right,  $n = 257$ ) cells. Glutamate was correlated with GABA and glutamine (inset). Two-sided Pearson's correlation analysis was performed.  $P$  values were not adjusted. For (**c–e**), Source data are provided as Source Data files.

(Supplementary Fig. 2a, b). For each cell, the DCFDA intensity and the abundance of metabolites were concomitantly collected. Then the correlation between DCFDA intensity and metabolite abundance was analyzed, with the calculation of Pearson's  $r$  coefficient to assess the strength of the correlation. For example, the intracellular GSH abundance exhibited an inverse correlation with the DCFDA intensity in the cells (Fig. 2a). The consistency with previous studies, which highlight the pivotal role of GSH as a crucial metabolite in maintaining redox balance<sup>29,30</sup>, further confirms our method's reliability.

Among the whole metabolome, we observed a total of 254 metabolites significantly correlated with OS level ( $P < 0.05$ ). The majority (61.4%) of the metabolites correlated with OS level ( $P < 0.05$ ) exhibited an inverse correlation, which is nearly double the number of metabolites that showed a positive correlation with cellular OS. This suggests that the downregulation of multiple metabolites may serve as a crucial hallmark of OS (Fig. 2b). For instance, the abundance of key metabolites associated with energy metabolism, such as ATP (Fig. 2c) and phosphocreatine (Fig. 2d), exhibited a progressive decline as OS level increased. The linear downregulation was also observed in other high energy compounds such as uridine triphosphate (UTP) and guanosine triphosphate (GTP) (Fig. 2e, f). The abundance of hypotaurine (HypT), which generates NADH as a by-product upon conversion to taurine<sup>31</sup> and plays crucial roles in redox homeostasis and DNA protection<sup>32</sup>, gradually declines during OS (Fig. 2g). The energy metabolism is composed of numerous metabolites and is detrimentally affected by OS<sup>33</sup>. Single-cell energy charge, a metabolic parameter used to assess cellular energy supply by measuring ATP, ADP and adenosine monophosphate (AMP) levels, reflects the energy homeostasis within a cell<sup>34</sup>. The inverse correlation observed between the single-cell energy charge and the cellular OS level (Fig. 2h) indeed suggests an association between OS and dysfunctionality in energy metabolism.

By performing the metabolite set enrichment analysis (MSEA)<sup>35</sup> using the metabolites inversely correlated with OS level, we found a variety of metabolic pathways related to different biological processes were disturbed in OS (Fig. 2i), such as the mitochondrial and energy metabolism including “Mitochondrial Electron Transport Chain” and “Citric Acid Cycle”, and the redox metabolism including “Glutathione Metabolism Pathway”. These findings were in consistence with previous reports observing the disruption of glutathione metabolism<sup>36,37</sup> and energy metabolism<sup>33</sup> during OS. Lipid metabolism has been reported to be altered in OS<sup>38,39</sup>. This was also verified by our finding of the downregulated pathways such as “Phosphatidylethanolamine Biosynthesis”, “Phosphatidylcholine Biosynthesis”, and “Sphingolipid metabolism”. The downregulation of purine and pyrimidine metabolic pathways revealed by the SCLIMS was also supported by previous studies reporting a depletion of purine and pyrimidine nucleotide during OS<sup>40</sup>. The SCLIMS also revealed an interference of vitamin metabolic pathways including “Thiamine Metabolism Pathway” and “Riboflavin Metabolism Pathway” during OS, which is in line with previous studies illustrating the crucial role of thiamine and riboflavin in regulating OS<sup>41,42</sup>. The consistency of these discoveries by SCLIMS and previous reports again suggests the reliability of the technique.

The SCLIMS additionally detected numerous previously undisclosed metabolic alterations during OS. For instance, pathways

related to amino acids metabolism such as “glutamate metabolism”, “alanine metabolism”, “arginine and proline metabolism” were all disturbed in the cells with OS. Moreover, pathways related to sugar and derivatives metabolism such as “Amino sugar metabolism”, “Fructose and mannose degradation”, “Lactose synthesis”, “Lactose degradation”, and “Nucleotide sugars metabolism” were also discovered to be downregulated in OS. Other pathways like “threonine and 2-oxobutanoate degradation” were also found to be disturbed in OS (Fig. 2i). The discoveries made by SCLIMS have shed light on the pivotal role of metabolism in cellular oxidative stress, unveiling a diverse array of metabolic pathways that undergo significant alterations ( $P < 0.05$ ). These findings indicate that the mechanisms governing protein synthesis and degradation, glycosylation reactions, and energy metabolism may undergo drastic transformations under OS.

The SCLIMS technique was also employed for multi-modal analysis in MEFs. Firstly, the metabolomics data were validated for the absence of any noticeable batch effect through PCA and HCA (Supplementary Fig. 2c, d). In MEFs, the key metabolites found to be inversely correlated with OS levels in HEK cells, including GSH, O-PE, CTP, ATP, UTP, HypT, GTP, and PCr, were similarly observed to exhibit reverse correlation with single-cell OS levels (Supplementary Fig. 3a). Additionally, MSEA analysis was conducted using these metabolites exhibiting inverse correlation with OS levels to unravel the metabolic pathways involved in oxidative stress of MEFs. Similar to the results of HEK cells, a variety of metabolic pathways were enriched (Supplementary Fig. 3b). For example, “Pyruvate metabolism”, “Citric acid cycle”, “Beta oxidation of very long chain fatty acids”, and “Mitochondrial electron transport chain”, in mitochondria and energy metabolism were also involved in the OS of MEFs. Lipid metabolism, including “Phosphatidylcholine Biosynthesis”, “Phosphatidylethanolamine Biosynthesis”, “Sphingolipid metabolism”, were altered during OS in MEFs as well. The downregulation of purine and pyrimidine metabolic pathways were also discovered in MEFs under OS. Similar to the interruption of vitamin metabolism in HEK cells under OS, “Pantothenate and CoA Biosynthesis”, “Thiamine Metabolism Pathway” were also discovered to be downregulated in OS-stressed MEFs. The outcomes in other pathways also exhibited a resemblance to those observed in HEK cells. These results confirmed the robustness of the multi-modal analysis of SCLIMS across diverse cellular phenotypes.

Taken together, revealing a profound interplay, the SCLIMS-based cross-modality analysis has unveiled strong connections between single-cell metabolism and OS, thereby highlighting the paramount importance of integrating metabolome and cellular phenotype for comprehensive insights across different cell types.

### Cell types identified by the SCLIMS exhibit divergent OS levels

Cluster analysis was conducted using k-medoids algorithm<sup>43,44</sup> based on the single-cell metabolome acquired from the SCLIMS. As a result, cells were clustered into six subtypes (C1–C6) with distinct metabolic features according to their metabolome profiles, highlighting the diversity of metabolic characteristics within these cells (Fig. 3a). Notably, the six subtypes of cells displayed distinct levels of OS as indicated by varying DCFDA intensities (Fig. 3b). We then performed a pseudotime analysis using single-cell metabolomics data and generated a trajectory of the six subtypes. The trajectory originated from



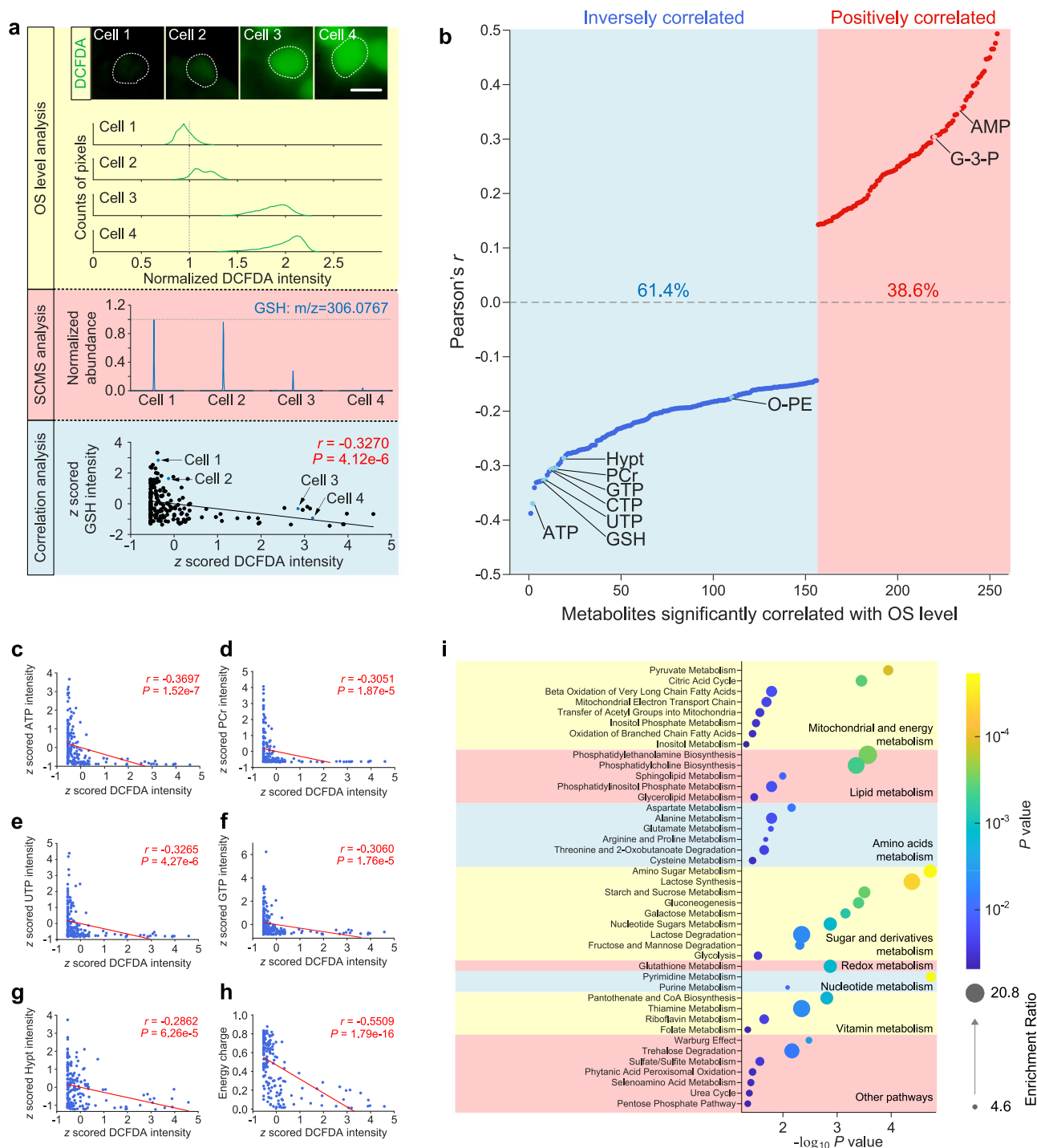


**Fig. 2 | The correlation analysis of intracellular metabolome and cellular OS level.** **a** The diagram illustrates the pairing of metabolic data and OS levels, as well as the subsequent correlation analysis. The DCFDA intensity indicated the specific level of OS in each cell, while single-cell MS was employed to determine the abundance of metabolites. Here, the metabolite GSH in Cells 1–4 was used as an illustrative example. Data from Cell 1–4 was normalized to Cell 1. The vectors for  $x$  and  $y$  were constructed based on single-cell OS levels and metabolite abundances, followed by calculation of Pearson's coefficient ( $r$ ) and significance ( $P$ ). In correlation analysis, the data was  $z$  scored. Scale bar, 15  $\mu\text{m}$ . **b** Metabolites that were inversely and positively correlated with the level of OS. Metabolites are shown as dots by color: red, positively correlated ( $P < 0.05$ ); blue, inversely correlated ( $P < 0.05$ ). The representative metabolites are annotated adjacent to the corresponding dots.  $P$  values were not adjusted. Two-sided Pearson's correlation analysis was performed. **c–h** The correlation analysis between the scaled levels of OS and

the scaled intensities of representative metabolites including ATP (c), PCr (d), UTP (e), GTP (f), Hypt (g), and energy charge (h). The data were standardized by calculating  $z$  score.  $P$  values were not adjusted. Two-sided Pearson's correlation analysis was performed. **i** The metabolic pathways enriched by the MSEA analysis of metabolites exhibiting a reverse correlation with OS levels. Only metabolites with MS/MS confirmation were included in the analysis. Only pathways with  $P < 0.05$  in the MSEA analysis were included.  $P$  values were not adjusted. Related metabolic processes are annotated on the left. Dot size represents enrichment ratio, and dot color represents significance of the enrichment ( $P$  value). Yellow, relatively high significance; Blue, relatively low significance.  $n = 190$  cells in (a) and (c–h). For (a–h), Source data are provided as Source Data files. ATP adenosine triphosphate, PCr phosphocreatine, UTP uridine triphosphate, GTP guanosine triphosphate, Hypt hypotaurine, GSH glutathione, CTP cytosine triphosphate, O-PE O-phosphoethanolamine, G-3-P glycerol 3-phosphate, AMP adenosine monophosphate.

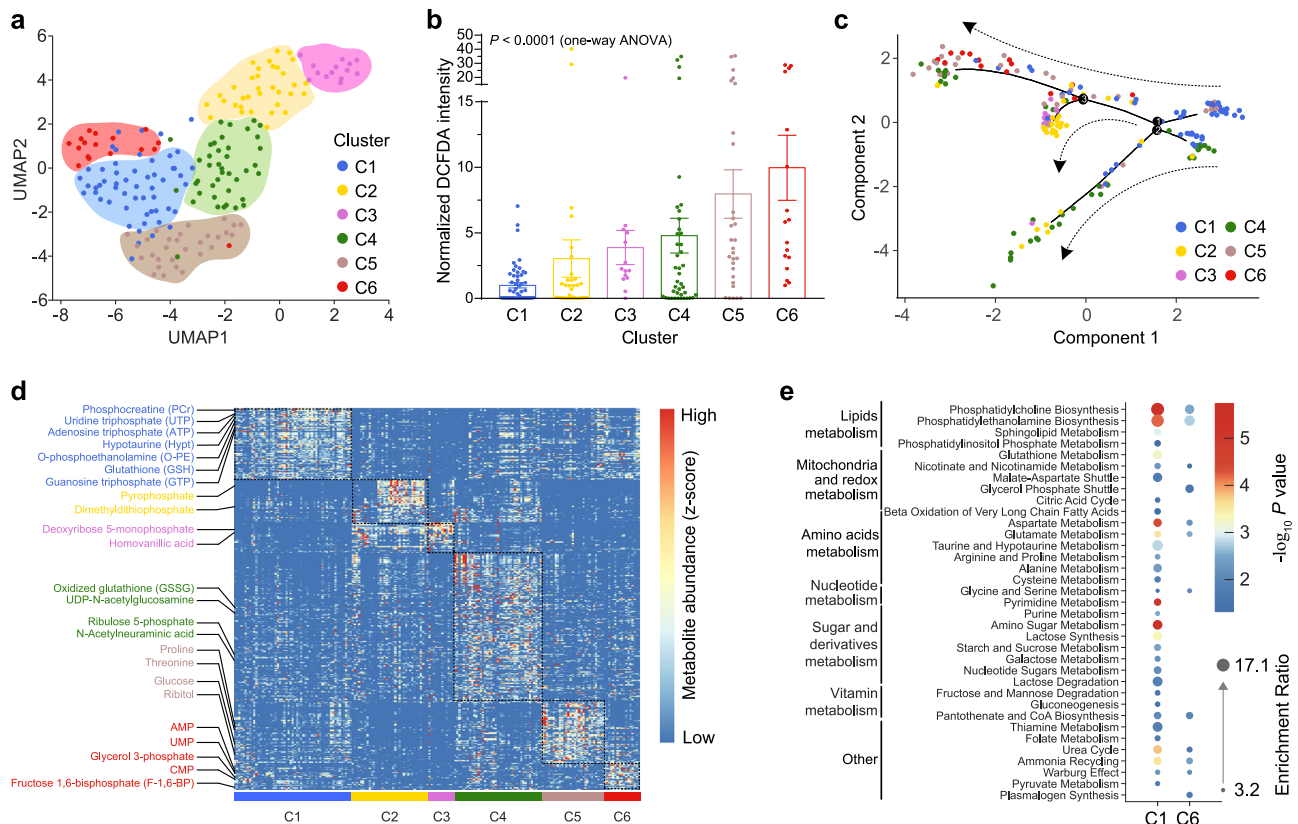


**Fig. 3 | Subtype-specific metabolic signatures and dynamic change of metabolome revealed by cross-modality analysis. a** UMAP visualization of six cellular subtypes based on the single-cell metabolome. Each point represents a single cell, color represents different subtypes.  $n = 55, 34, 14, 41, 29$ , and  $17$  for C1, C2, C3, C4, C5, and C6 respectively. **b** Average OS levels (indicated by the normalized DCFDA fluorescence intensity) of the six metabolic subpopulations.  $n = 55, 34, 14, 41, 29$ , and  $17$  for C1, C2, C3, C4, C5, and C6, respectively.  $F(5, 184) = 5.880$ ,  $P = 4.57 \times 10^{-5}$  in One-way ANOVA (labeled in the plot). Data was normalized to values of the respective control (Cluster C1). Data is presented as mean  $\pm$  s.e.m. Color represents different subtypes and each dot represents a cell. **c** Single-cell trajectory of pseudotime analysis showing temporal progression of cell subtypes originating from C1 and gradually transitioning

towards C2/3, C4, and C5/6. Each subtype is represented by a distinct color. For (a–c), Blue: C1; yellow: C2; purple: C3; green: C4; brown: C5; red: C6. **d** Heatmap of characteristic metabolites and their corresponding relative intensities in each subtype. Color indicates z-scores of metabolite abundance. Red: relatively high abundance; blue: relatively low abundance. **e** Representative metabolic pathways significantly ( $P < 0.05$ ) enriched in Cluster C1 and C6 through the MSEA analysis. Only metabolites with MS/MS confirmation were included in the analysis. Dot size represents enrichment ratio, while dot color indicates significance ( $-\log_{10} P$  value) of the enrichment. Red: relatively high significance; blue: relatively low significance.  $P$  values were not adjusted. For (a–c), Source data are provided as Source Data files. Data was collected from at least three biological replicates.

subtype C1, which exhibited the lowest level of OS, and gradually progressed towards other subtypes. Notably, three distinct branches were observed that led to C2/3 (representing a low oxidative level), C4 (representing a medium oxidative level), and C5/6 (representing a high oxidative level), respectively (Fig. 3c). These findings suggest a metabolism-guided stepwise progression of cellular OS.

We subsequently conducted a more detailed analysis of the six metabolic subtypes by utilizing a Wilcoxon rank sum test to compare metabolite abundance between each cluster and other clusters. Each subtype was characterized with specific metabolic markers as shown in the heatmap (Fig. 3d). For instance, cells of Cluster C1 exhibited enrichment of energy rich phosphate compounds such as ATP, GTP, UTP, phosphocreatine along with antioxidants including GSH; cells of Cluster C2 were enriched with dimethyldithiophosphate and pyrophosphate; cells of Cluster C3 showed an abundance of catecholamine derivatives such as homovanillic acid and sugar derivatives such as deoxyribose 5-phosphate; cells of Cluster C4 were enriched with intermediates of nucleotide metabolism such as guanine monophosphate (GMP), along with acetylated compounds such as N-acetylneuraminic acid and UDP-N-acetylglucosamine; cells of Cluster C5 were enriched with amino acids such as proline, threonine, asparagine, alanine and taurine, along with glucose and ribitol;

Nucleotide monophosphates, including AMP, cytidine monophosphate (CMP), and uridine monophosphate (UMP), as well as intermediates in the glycolysis pathway (i.e. glyceraldehyde 3-phosphate and fructose 1,6-bisphosphate), were found to be enriched in cells belonging to Cluster C6.

Next, we conducted a comparison of the metabolome at the single-cell level between Cluster C6 (with the most oxidative level) and Cluster C1 (with the least oxidative level). A total of 148 metabolites were downregulated and only 64 metabolites were upregulated from C1 cells to C6 cells (Supplementary Fig. 4a). To investigate the alteration of the metabolic process in cellular OS, we performed the MSEA analysis of the characteristic metabolites enriched in C1 and C6 cells (Fig. 3e), and other clusters of cells (Supplementary Fig. 5). Specifically, pathways related to lipid metabolism such as “Phosphatidylethanolamine Biosynthesis”, “Phosphatidylcholine Biosynthesis”, “Sphingolipid Metabolism”, and “Phosphatidylinositol Phosphate Metabolism” were less enriched or completely depleted in C6 cells, consistent with previous reports<sup>38,39</sup>. The pathways associated with mitochondrial function and redox balance, such as “Citric Acid Cycle”, “Nicotinate and nicotinamide metabolism” and “Glutathione metabolism” were also found to be depleted or less enriched in cells of C6, thus confirming previous reports on the disruption of glutathione metabolism<sup>36,37</sup> and

energy metabolism<sup>33</sup> under OS. The pathways related to metabolism of sulfinic acids and organosulfonic acids, such as hypotaurine and taurine metabolism, were depleted in C6 cells. This was supported by studies illustrating the antioxidant effect of these metabolites<sup>45,46</sup>. In addition, the glycine and serine metabolism exhibited greater enrichment in C6 cells, which may be a compensatory response of cells under OS as glycine and serine metabolism are reported to attenuate OS in *C. elegans*<sup>47</sup>. The nucleotide metabolism pathways, such as “Purine metabolism” and “Pyrimidine metabolism”, were depleted in C6 cells. The metabolism of vitamins, including “Pantothenate and CoA metabolism”, “Thiamine metabolism”, and “Folate metabolism”, exhibited reduced enrichment or depletion in C6 cells. The alteration of nucleotide and vitamin metabolism in OS were well described by previous researches<sup>40–42</sup>. Other pathways such as “Plasmalogen Synthesis” was enriched exclusively in the cells of C6 (Fig. 3e). Plasmalogen synthesis is reported to enhance the resistance to OS in *E. Coli*<sup>48</sup>, which could be served as a protective response in cells under OS. Together, the convergence of these consistent findings between the SCLIMS and the existing literature further substantiates the dependability and steadfastness of this technique.

Moreover, the SCLIMS has also unearthed previously unreported perturbed pathways during OS. For instance, several metabolic pathways, such as “Fructose and mannose degradation”, “Amino sugar metabolism”, “Nucleotide sugars metabolism” along with amino acids metabolism including “alanine metabolism”, “glutamate metabolism”, and “arginine and proline metabolism”, were identified to be implicated in OS, which has not been elucidated in previous studies. Another finding gleaned from the SCLIMS is the transition from the “Malate-Aspartate Shuttle” pathway to the “Glycerol Phosphate Shuttle” pathway, observed between C1 and C6, implying a reduced efficiency in ATP generation during OS.

The metabolic heterogeneity of MEFs under OS was meticulously investigated using SCLIMS, revealing a parallel to HEK293T cells where six distinct subtypes (M1–M6) with specific metabolic characteristics were identified (Supplementary Fig. 6a). These subtypes in MEFs also exhibited varying levels of OS (Supplementary Fig. 6b). Furthermore, pseudotime analysis utilizing single-cell metabolic features unveiled a trajectory of the six subtypes originating from M1 (with the lowest level of OS) and progressing towards M3 (with moderate OS), followed by M5 and finally converging at M4/6 (with higher levels of OS) (Supplementary Fig. 6c). Notably, a metabolism-guided progression of cellular oxidative stress was similarly observed in MEFs.

The metabolite abundance was also analyzed between each cluster and other clusters, revealing subtype-specific metabolic markers (Supplementary Fig. 6d). In comparison to HEK293T cells, MEFs exhibited strikingly similar metabolic characteristics. Similar to C1 in HEK293T cells, M1 in MEFs shared crucial metabolites such as Hypt, PCr, O-PE, ATP, GTP, UTP, and GSH. Both C1 and M1 displayed the lowest level of OS. A comparison of the metabolites in M6 (with the highest OS level) and M1 (with the lowest OS level) yielded a result akin to that observed in HEK293T cells. A total of 195 metabolites were downregulated, while 134 metabolites were upregulated from M1 to M6 (Supplementary Fig. 4b). The metabolic pathways enriched in M1 and M6 were also analyzed using MSEA and compared (Supplementary Fig. 6e). Consistent with the findings in C1 and C6 of HEK293T cells, common lipid metabolic pathways such as “Phosphatidylethanolamine Biosynthesis”, “Phosphatidylcholine Biosynthesis”, and “Sphingolipid Metabolism” exhibited depletion in M6 MEFs characterized by the highest level of OS. Additionally, key pathways involved in mitochondrial function and redox balance, namely “Citric Acid Cycle” and “Glutathione metabolism”, were also found to be depleted in M6 MEFs. Furthermore, several other pathways including “taurine and hypotaurine metabolism”, “alanine metabolism”, “glutamate metabolism”, and “arginine and proline metabolism” were identified as being implicated specifically in the OS subtype of MEFs at stage M6.

Similarly, nucleotide metabolism pathways including “Purine metabolism” and “Pyrimidine metabolism” showed depletion or less significant enrichment in the same group of cells. Moreover, there was a depletion observed in the vitamin-related metabolic processes such as “Pantothenate and CoA metabolism”, “Thiamine metabolism”, and “Folate metabolism” within the context of OS progression among these specific type of cells. The obtained results exhibited consistency with those observed in HEK293T cells, as well as previous studies that have dissected cellular OS metabolism mentioned above. Consequently, SCLIMS has been demonstrated to possess robustness in analyzing metabolic alterations at the single-cell level.

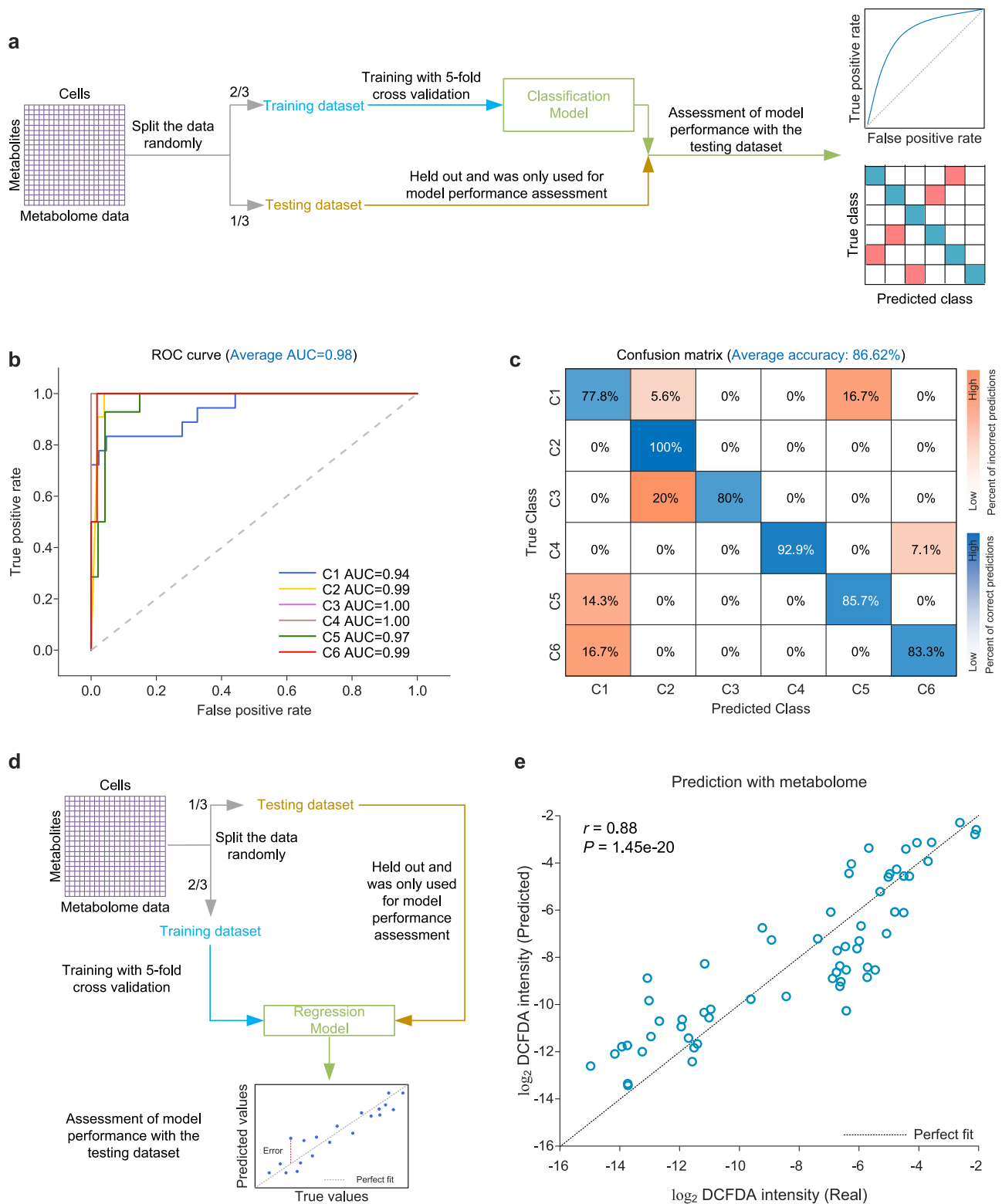
Taken collectively, the SCLIMS not only validate metabolic changes observed in previous studies but also unveil metabolic modifications associated with OS and metabolic heterogeneity within individual cells. These findings emphasize the reliability and universality of this technique, establishing it as a powerful tool for comprehensive analysis at the single-cell level.

### The SCLIMS reveals capability of the single-cell metabolome in predicting cellular OS status

Although the metabolic alterations and heterogeneity of cells under OS were explored in detail, the strength of the link between metabolism and cellular phenotype is not fully established. Machine learning is utilized to ascertain whether the metabolic profile of individual cells can accurately predict heterogeneous subtypes with distinct OS levels. We employed discriminant analysis algorithms to train classification models using single-cell metabolic features aiming to distinguish the 6 subtypes with specific OS levels identified in the above-mentioned clustering analysis (Fig. 4a). The data was randomly divided into independent training and testing datasets, with 2/3 of the original data composing the former and 1/3 of it composing the latter. Both datasets included all m/z signals meeting our criteria ( $S/N > 3$  and detected in greater than 20% single cells) and no variable selection is performed before the model was trained. The model was trained on the training dataset to acquire the ability to classify metabolic subtypes based on full features of the single-cell metabolome, and its performance was assessed using the testing dataset. The performance of the model was evaluated using receiver operating characteristic (ROC) curve and confusion matrix. In multi-classification, the ROC curve had an average area under curve (AUC) of 0.98 (Fig. 4b). In cluster prediction, the model achieved an accuracy ranging from 77.8% to 100% (Fig. 4c). These results demonstrate that the single-cell metabolic profiles can directly predict metabolic subtypes.

The classification model is capable of predicting metabolic subtypes rather than precise levels of OS. We further trained a regression model<sup>49,50</sup> based on neuronal network algorithms (Fig. 4d), which may enable direct prediction of single-cell OS levels utilizing metabolic features. Similarly, the data was independently and randomly divided into training and testing datasets, with 2/3 of the original data comprising the former and 1/3 comprising the latter. All m/z signals meeting our criteria ( $S/N > 3$  and detected in greater than 20% single cells) were included in building the regression model without variable selection. The model was trained on the training dataset to predict single-cell OS levels, as manifested by DCFDA intensity, based on single-cell metabolic features. The performance of the model was evaluated with the testing dataset, and the predicted values were plotted against real values (Fig. 4e). The correlation coefficient ( $r$ ) was 0.88, indicating a good predictive power of the model. Furthermore, the metabolic profile of single-cells was further validated in MEFs, demonstrating a high predictive power with an AUC of 0.99 and an average accuracy of 88.42% in the classification model (Supplementary Fig. 7a, b). Additionally, there was a significant correlation between predicted and true OS levels ( $r = 0.6$ ,  $P < 0.0001$ ) as shown in the correlation analysis (Supplementary Fig. 7c).

Thus, through the implementation of SCLIMS technique and its multi-modal integration, we have successfully demonstrated a link



between single-cell metabolome and cellular OS states in two different cell types for the very first time, suggesting the potential role of metabolome in determining cellular phenotype.

### The SCLIMS unveils the causal relationship between metabolic heterogeneity and OS status

Although there appears to be a strong correlation between the heterogeneity of OS levels and metabolic heterogeneity, the causal relationship between them remains unclear. We wonder if the baseline

metabolic profile determines the phenotypic or metabolic heterogeneity of cells after they are induced to OS. We define the cells prior to OS induction with hydrogen peroxide as “initial cells”, representing the baseline state of both metabolism and phenotype. With SCLIMS, we analyzed the heterogeneity of the OS levels and the single-cell metabolome in the initial cells untreated with  $H_2O_2$ . We surprisingly found that while there was minimal heterogeneity in cellular OS levels among the initial cells (Fig. 5a and Supplementary Table 1), there existed heterogeneity in their single-cell metabolome (Fig. 5b, c).



**Fig. 4 | Machine learning-guided prediction of OS levels based on single-cell metabolome.** **a** Flowchart of classification analysis with machine learning. The training and testing dataset were randomly assigned according to a ratio of 2:1. The model was trained and built with the training dataset with 5-fold cross validation. The testing dataset was held out and used for the evaluation of model accuracy independently. The performance of the model was evaluated with ROC curve and confusion matrix. **b** ROC curve of model testing. AUC for each cluster was determined separately by the classification model. Higher AUC value indicates a better performance of the model in predicting the clusters. The average AUC represented an overall performance of the model. The color represents classification of a certain subtype. Blue: C1; yellow: C2; purple: C3; brown: C4; green: C5; red: C6. **c** Confusion matrix of model testing, illustrating the distribution of errors in multi-class

prediction. The average accuracy was used to evaluate the overall performance of the model. The color depth indicates the proportion of correct (blue) and incorrect (red) predictions, as displayed in the bar chart. **d** Flowchart of building a regression model with machine learning. The training and testing datasets were randomly assigned according to a ratio of 2:1. The model was trained and built with the training dataset with 5-fold cross validation. The testing dataset was held out and used for the evaluation of the model independently. **e** The correlation of real values and values predicted by the regression model ( $n = 61$ ). Dash line represents the perfect fit (predicted values = real values). The model performance was evaluated by the correlation coefficient ( $r$ ) and  $P$  value ( $P$ ). Two-sided Pearson's correlation analysis was performed.  $P = 1.45 \times 10^{-20}$ .  $P$  value was not adjusted. For **b** and **e**, Source data are provided as Source Data files. AUC area under curve.

Specifically, the k-medoids clustering analysis revealed two major metabolic subtypes (Cluster-I and Cluster-II) in the initial cells based on their metabolomics features (Fig. 5b). Through machine learning, the single-cell metabolome can directly predict the subtype of a cell, providing further evidence for the robust heterogeneity of metabolism in the initial cells (Supplementary Fig. 8a, b). To investigate metabolic properties of the two subtypes of initial cells, we performed a differential analysis by comparing metabolite abundance between Cluster-I and Cluster-II cells. A series of characteristic metabolites, such as hypotaurine, GSH, ATP, UTP, O-phosphoethanolamine, and GSSG, distinguishing the two subtypes were discovered (Fig. 5c).

Interestingly, despite no initial cells being subjected to OS stimulation, the metabolic disparity between the two cell subtypes in these initial cells already demonstrated a consistent pattern with the metabolic variation observed in cells with varying levels of OS. Specifically, the metabolomic similarity between single cells was determined by calculating the statistical distance of their metabolomic data. The initial cells (from Cluster-I and Cluster-II) were paired with each cell under OS (from C1–C6), and subsequently, the distance was computed based on the metabolite abundance in the two cells. A larger value of statistical distance indicates a lower degree of similarity<sup>6</sup>. The heatmap visualization (Fig. 5d) was generated based on the reciprocal value of statistical distance, which represents the level of similarity among single cells. From a metabolomic perspective, cells in Cluster-II exhibit greater similarity to cells with higher levels of OS (i.e., C2–4), while cells in Cluster-I are more similar to cells with lower levels of OS (i.e., C1) (Fig. 5d). The abundance of GSH, ATP and hypotaurine were 82%, 42%, and 87% lower in cells of Cluster-II (Fig. 5e, f and Supplementary Fig. 8c), which was in line with the above-mentioned downregulation of GSH, ATP, and hypotaurine discovered in cells with high OS levels (Supplementary Fig. 4). Metabolic pathways including “Glutathione metabolism”, “Phosphatidylcholine Biosynthesis”, “Phosphatidylethanolamine Biosynthesis”, “Sphingolipid Metabolism”, “Pyrimidine Metabolism”, “Purine Metabolism”, “Thiamine Metabolism”, “Pantothenate and CoA Biosynthesis”, and “Taurine and Hypotaurine Metabolism” were enriched with marker metabolites in cells of Cluster-I (Supplementary Fig. 8d). Notably, these pathways were all downregulated in cells with high OS levels (i.e., cells in C6) when compared to cells with low OS levels (i.e., cells in C1) (Fig. 3e).

A remarkable demonstration of the metabolic heterogeneity exhibited by initial cells is exemplified by GSH. The UMAP map vividly depicted the remarkable disparity in GSH abundance among individual cells of Cluster-I and Cluster-II (Fig. 5e). We further constructed metabolic networks based by leveraging the correlation among metabolites. The correlations between metabolites exhibited alterations in cells belonging to Cluster-I and Cluster-II, indicating a subtype-specific metabolic profile. For instance, the intracellular level of GSH was strongly correlated with 15 other metabolites in Cluster-I, whereas only 5 metabolites displayed a correlation ( $r > 0.8$ ,  $P < 0.05$ ) with GSH in Cluster-II (Fig. 5g), indicating a notable divergence in the GSH-centered network between the two cell subtypes. The DyNet algorithm was employed to calculate the rewiring score<sup>51</sup> for each metabolite in

Cluster-I and Cluster-II networks, which quantifies modifications in a specific metabolite's correlation with other metabolites between the two clusters. Notably, the identification of GSH as the most rewired metabolite (Fig. 5h) highlights its pivotal role in connecting with other metabolites within the metabolome.

The metabolic heterogeneity in initial MEFs was also investigated. Notably, MEFs were classified into two distinct subtypes (Cluster-1 and Cluster-2) exhibiting metabolic characteristics akin to the two clusters observed in initial HEK293T cells (Cluster-I and Cluster-II) (Supplementary Fig. 9a, b). The detailed metabolic properties of Cluster-1 and Cluster-2 initial MEFs were further studied. Several key metabolites, including Hypt, GSH, O-PE, and ATP exhibited enrichment in Cluster-1 within the initial MEFs, aligning with the characteristic metabolites in Cluster-I within the initial HEK293T cells. The Pathways including “Glutathione metabolism”, “Phosphatidylcholine Biosynthesis”, “Phosphatidylethanolamine Biosynthesis”, “Sphingolipid Metabolism”, “Pyrimidine Metabolism”, “Purine Metabolism”, “Thiamine Metabolism”, “Pantothenate and CoA Biosynthesis”, and “Taurine and Hypotaurine Metabolism” were enriched with marker metabolites in Cluster-1 cells (Supplementary Fig. 10c), which was consistent with the pathways enriched in Cluster-I in HEK293T cells (Supplementary Fig. 8d). These pathways were also depleted or less enriched in MEFs with the highest OS levels (Cluster-M6). Machine learning analysis of the single-cell metabolome of initial MEFs confirmed the robust heterogeneity in cellular metabolism (Supplementary Fig. 10a, b). We next calculated the metabolic similarity between Cluster-1 and Cluster-2 initial MEFs in the absence of OS with the M1–M6 MEFs under OS conditions. Similarly, Cluster-1 initial MEFs exhibited a higher degree of similarity to MEFs with lower levels of OS, such as M1, M2, and part of M3 (Supplementary Fig. 9c). On the other hand, Cluster-2 initial MEFs showed a greater resemblance to MEFs with higher levels of OS including M4, M5, and M6 (Supplementary Fig. 9c). These findings were consistent with the results observed in HEK293T cells.

Next, the role of GSH in distinguishing the metabolic landscape of Cluster-1 and Cluster-2 was confirmed in the initial MEFs. As shown in Supplementary Fig. 9d, e, Cluster-1 exhibited higher levels of GSH abundance, which could potentially serve as a discriminative factor between the two clusters. Metabolic networks were constructed for both Cluster-1 and Cluster-2 based on metabolite correlations (Supplementary Fig. 9f). Similar to the networks observed in HEK293T cells for Cluster-I and Cluster-II, it was found that compared to Cluster-2, Cluster-1 displayed a more intricate network connectivity among metabolites, indicating a subtype-specific metabolic profile within the initial MEFs. Furthermore, the key role of GSH in governing metabolism and correlation between metabolites, as well as its ability to distinguish between the two subtypes of initial MEFs, were also elucidated. These findings align with the observed role of GSH in initial HEK293T cells. Moreover, the divergence in the GSH-centered network between these two cell subtypes was confirmed in initial MEFs. By employing the DyNet algorithm to compare the two metabolic networks, GSH emerged as the fourth-highest rewired metabolite (Supplementary Fig. 9g). These results underscored both

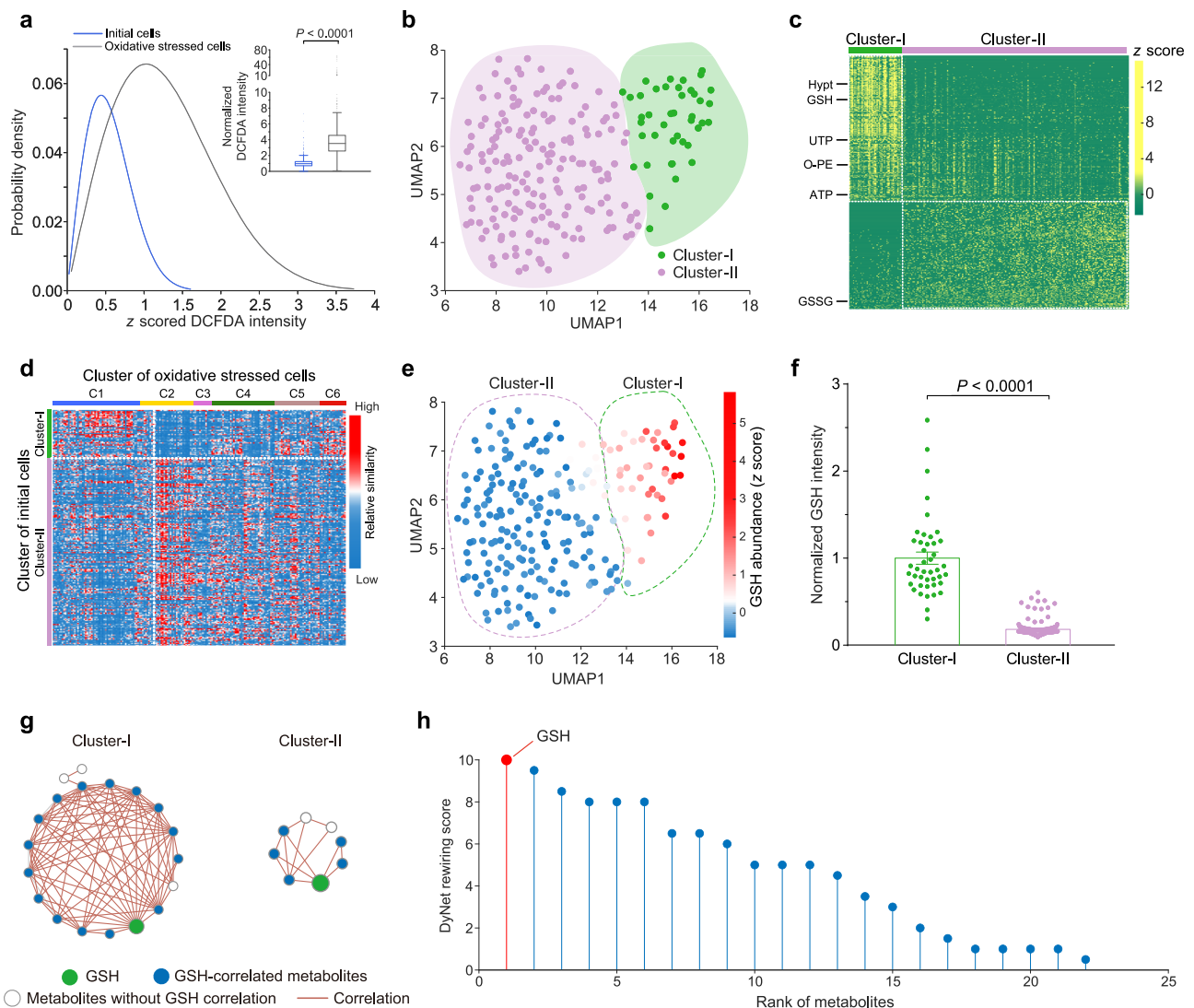


**Fig. 5 | Metabolic heterogeneity in initial cells.** **a** Distribution and box plot (inset) of DCFDA intensity in initial cells and cells under OS. Data in distribution plot was z scored. Variance was indicated by IQR and MAD values in Supplementary Table 1.  $W = 58627$ ,  $P < 2.2 \times 10^{-16}$  in unpaired two-tailed Wilcoxon rank sum test. The data presented in the inset was normalized to the values of initial cells. Box plots extend from 25th to 75th percentiles; central lines represent medians; whiskers extend over 1.5 times the interquartile range (IQR, the distance from 25th to 75th percentile); dots represent outliers. For single-cell DCFDA intensity, a total of 1740 initial cells (blue) and 960 oxidative stressed cells (gray) from 3 independent experiments were analyzed. **b** UMAP visualization of metabolic subtypes in initial cells. Green: cells of Cluster-I ( $n = 43$ ). Purple: cells of Cluster-II ( $n = 183$ ). **c** Heatmap of potential metabolic markers in Cluster-I and Cluster-II. The data was z score scaled. The color represents relative abundance of metabolites. Yellow: relatively high abundance; green: relatively low abundance. Each row represents a metabolite and each column represents a cell. The representative metabolites are labeled on the left and the clusters are labeled on the top. ATP: adenosine triphosphate; GSH: glutathione; GSSG: oxidized glutathione; HypT: hypotaurine; O-PE: O-phosphoethanolamine; UTP: uridine triphosphate. **d** A heatmap illustrating the metabolic similarity between subtypes of initial cells (Cluster-I/II) and subtypes of oxidative stressed cells (C1 to C6). Each row represents an initial cell (subtypes are labeled on the left) and each column represents an oxidative stressed cell (subtypes are labeled on the top). The color represents relative similarity: red, relative high similarity; blue, relative low similarity. Cells of Cluster-I is more similar to the cells with lower OS levels (cells of C1 and part of C2). **e** Enrichment of GSH in cells of Cluster-I visualized on the UMAP plot. Each dot represents a cell, the color of the dots represents the relative GSH abundance. Red: relatively high abundance; blue: relatively low abundance. Data was z score scaled. **f** Quantification of GSH abundance in Cluster-I ( $n = 43$ , green) and Cluster-II ( $n = 183$ , purple). Data was normalized to values in Cluster-I. Data is represented as mean  $\pm$  s.e.m. Data were collected from at least three biological replicates.  $W = 7843$ ,  $P = 5.85 \times 10^{-43}$  in unpaired two-tailed Wilcoxon rank sum test. **g** The correlation of every two metabolites were calculated (reflected as Pearson's  $r$ ) and the network was constructed based on the correlation data for initial cells belonging to Cluster-I (left) and Cluster-II (right) subtypes. In the network, each node represents a metabolite while an edge connecting two nodes indicates their correlation. The big green dot denotes GSH and the small blue dots denote GSH correlated metabolites. Blank-colored dots indicate metabolites without any correlation to GSH. **h** Rewiring score calculated with DyNet algorithm. Metabolites with higher scores were more rewired in topology in the correlation network of initial cells. For (a, b, e, f), Source data are provided as Source Data files. GSH: glutathione.

the generality and reliability of the SCLIMS technique while demonstrating its applicability across diverse cell types.

In summary, utilizing the SCLIMS technique has revealed that while there was no obvious heterogeneity in initial cells at the OS level,

the metabolome exhibited a high degree of heterogeneity. Interestingly, this metabolic diversity in initial cells mirrored that observed in cells with varying OS levels, suggesting that it may be the root cause of heterogeneous OS levels within cells.

## The metabolic heterogeneity of cells determines their senescence fate under OS

A common fate of cellular OS is the oxidative stress-induced premature senescence, which is a crucial type of cellular senescence<sup>21–24,52</sup>. Subsequently, our objective was to identify a live-cell probe capable of distinguishing between the cells belonging to the two distinct metabolic subtypes, enabling us to further investigate their respective cellular fates in OS-induced senescence. The disparity in GSH levels between the two metabolic subtypes (Fig. 5e) prompted us to explore the potential of utilizing intracellular GSH levels as a means to distinguish between these two cell subtypes.

The initial cells exhibiting high/low (ranging from 5% to 50%) GSH levels were selected and mapped onto the UMAP projection alongside the remaining initial cells, followed by calculating the proportion of accurate matches between cells with high/low GSH levels and Cluster-I/II (Fig. 6a). The fraction of correct matches exhibited a drastic decline when the selection included more than 15% of cells with top/bottom GSH levels (Fig. 6b–g), suggesting that only cells within the range of 5%–15% accurately represented the metabolome of Cluster-I and Cluster-II, respectively, and potentially reflected resistance to OS and sensitivity to OS. To ensure stability, we carefully selected cells with the highest and lowest 5% GSH levels for further analysis, designating them as “initial cells exhibiting a metabolome resembling that of OS-resistant cells (C1)” (MROR cells) and “initial cells exhibiting a metabolome resembling that of OS-sensitive cells (C6)” (MROS cells).

To isolate the MROR and MROS cells, we employed a live-cell GSH fluorescent dye (monochlorobimane, mCIB)<sup>53</sup> and fluorescence activated cell sorting (FACS). The MROR cells (Top 5% fluorescent intensity) and the MROS cells (Bottom 5% fluorescent intensity) were collected by the FACS according to their mCIB fluorescent intensity (Fig. 6h and Supplementary Figs. 11, 12). The DCFDA intensity (Fig. 6i, j) had only 3% difference between MROR and MROS cells. However, following OS induction, the MROS cells exhibited 2.7-fold higher of DCFDA intensity compared to their MROR counterparts (Fig. 6i, j), indicating an elevated state of OS. Furthermore, SA- $\beta$ -Gal staining confirmed the sensitivity of MROS cells in OS-induced senescence (Fig. 6k, l). Thus, the data from the SCLIMS suggest that the metabolic features of an initial cell may dictate its destiny under OS and OS-induced senescence.

## The key metabolites identified by SCLIMS mitigate OS and cellular senescence

The aforementioned results suggest that the downregulation of critical metabolites, identified by the SCLIMS, may be a contributor to OS, indicating the potential for reversing OS and OS-induced senescence through targeted metabolite supplementation. To explore this possibility, we opted to conduct an experiment using three key metabolites: hypotaurine, phosphocreatine, and O-phosphoethanolamine, which all showed similar characteristics such as declining in OS (Fig. 2b), distributing heterogeneously across metabolic subtypes (C1–C6) (Fig. 3d), and serving as metabolic markers distinguishing the initial cells with different fates (Fig. 5c).

Treatment of cells with the three metabolites resulted in an average of 67% reduction in OS levels, as evidenced by a decrease in DCFDA intensity within the cells (Fig. 7a, b). OS is a common inducer of senescence<sup>22,54,55</sup> and also plays a vital role in natural aging<sup>56</sup>. We therefore explored the effects of these key metabolites on OS-induced senescence. The SA- $\beta$ -Gal staining showed that hypotaurine, phosphocreatine and O-phosphoethanolamine considerably decreased the cellular senescence (Fig. 7c, d and Supplementary Fig. 13a–c). The staining intensity exhibited an average of 48% reduction in key metabolite-treated cells compared with vehicle-treated OS cells. The growth arrest of cells, a marker for cellular senescence<sup>55,57</sup>, was also rescued by these metabolites (Fig. 7e, f and Supplementary Fig. 13d–f). The mitochondrial membrane potential (MMP), which is compromised

in cellular OS<sup>58,59</sup>, was recovered by targeted supplement of key metabolites (Fig. 7g, h). Furthermore, the examination of the three key metabolites on MEFs under OS yielded analogous outcomes, thereby indicating the generalized applicability of these key metabolites across diverse cell types (Supplementary Fig. 14). Collectively, these findings imply that the SCLIMS-identified metabolites exert a protective effect by reducing the OS level and alleviating senescence.

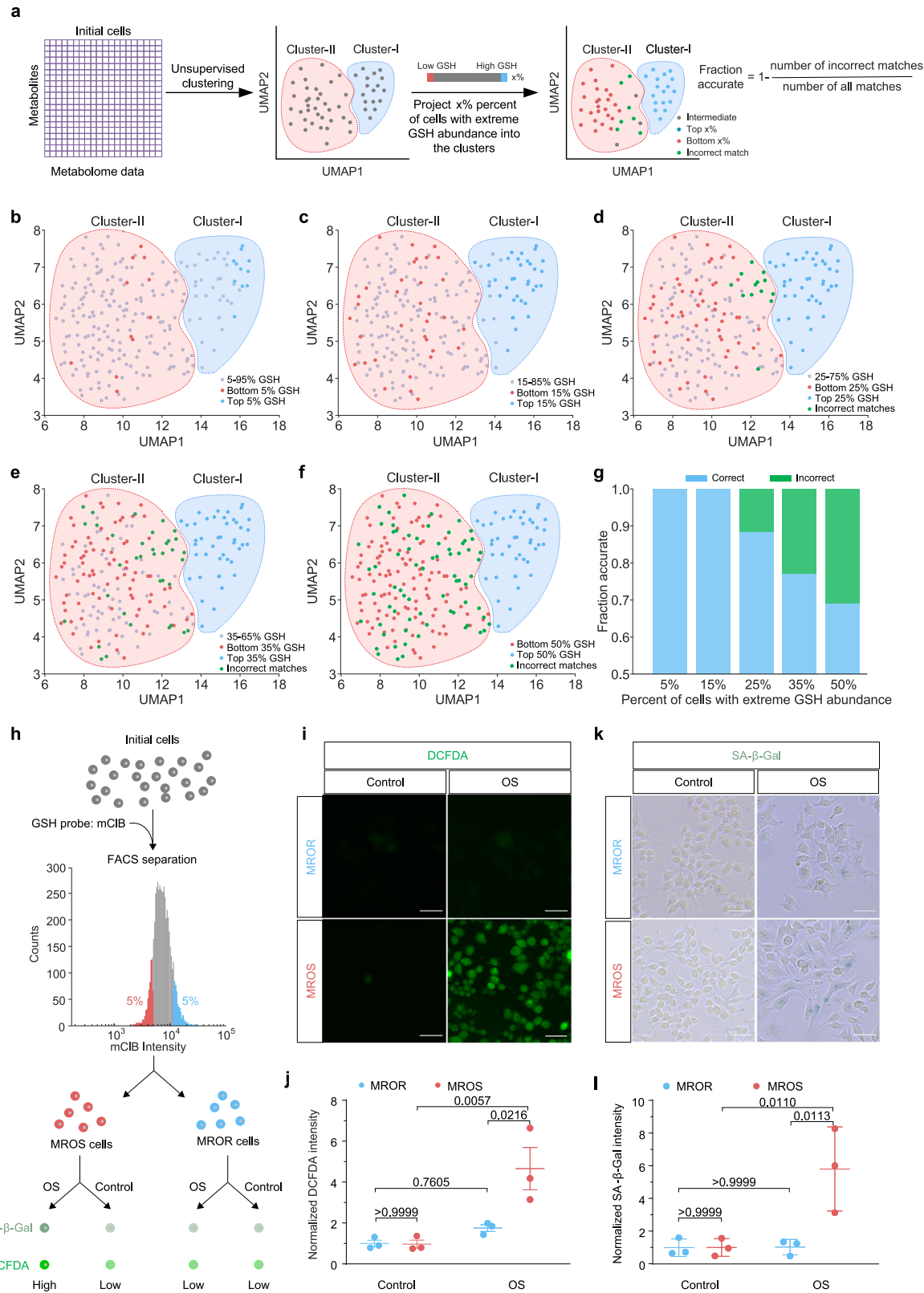
## Treatment of key metabolites regulated the metabolome of single cells

To investigate the precise alterations in the metabolome of individual cells upon treatment with key metabolites, we conducted metabolic analysis on cells from five groups: Non-OS, vehicle-treated OS, Hypo-treated OS, PCr-treated OS, and O-PE-treated OS. Subsequently, we examined the distinct metabolic characteristics exhibited by these cell populations (Supplementary Fig. 15a). Notably, cells treated with key metabolites were positioned between non-OS and vehicle-treated OS cells, indicating an intermediary metabolic state between the two groups. In consistency, cells treated with key metabolites exhibited intermediate intensity in DCFDA and SA- $\beta$ -Gal staining along with intermediate growth rate when compared to non-OS and OS cells (Fig. 7a–f). This suggests that the treatment of metabolites may have partially restored the disrupted metabolism in oxidative stressed cells and further alleviated cellular oxidative stress and senescence. To quantify the similarity between the metabolome of metabolite-treated cells and non-OS/OS cells, we calculated the paired distance between these cell types. Interestingly, compared to non-OS and OS cells, the cells treated with key metabolites exhibited a smaller distance to non-OS cells (Supplementary Fig. 15b). These findings indicate that treatment with key metabolites modulated the metabolome of OS cells towards a state similar to that of non-OS cells.

Next, the detailed alteration of metabolome in OS and metabolite-treated cells was further studied. By conducting a comparative analysis of metabolites in non-OS cells and those treated with OS, we identified a series of downregulated metabolites under OS conditions, which were subsequently restored upon treatment with key metabolites (Supplementary Fig. 15c). For instance, some key metabolites downregulated in OS, such as hypotaurine, phosphocreatine, O-phosphoethanolamine, GSH, ATP (Figs. 2b, 3d), were recovered under the treatment of hypotaurine, phosphocreatine, and O-phosphoethanolamine (Supplementary Fig. 15c). The metabolic pathways involved in the recovery of the metabolome were dissected through MSEA analysis using the recovered metabolites under treatment (Supplementary Fig. 15d). A subset of these metabolic pathways overlapped with those downregulated in OS. Specifically, the “Citric acid cycle” in mitochondrial metabolism; “Phosphatidylethanolamine Biosynthesis,” “Phosphatidylcholine Biosynthesis,” and “Sphingolipid Metabolism” in lipid metabolism; “Aspartate metabolism” and “Glutamate metabolism” in amino acid metabolism; “Pyrimidine metabolism” and “Purine metabolism” in nucleotide metabolism; and “Amino sugar metabolism,” “Galactose metabolism,” and “Nucleotide sugars metabolism” in sugar and derivatives metabolism were all enriched with recovered metabolites and overlapped with pathways downregulated in OS. Consistently, OS cells treated with key metabolites exhibited lower levels of OS, reduced SA- $\beta$ -Gal intensity, and improved mitochondrial function (Fig. 7 and Supplementary Fig. 14).

The collective findings suggest that the modulation of crucial metabolites governs the cellular metabolome under OS, leading to the restoration of a multitude of metabolites. Treatment with these pivotal metabolites induces a metabolic state resembling that of non-OS cells, thereby highlighting their significant role in regulating OS and senescence pathways. Consequently, it can be inferred that specific key metabolites exert control over the cellular metabolome. The observed extensive heterogeneity and metabolic disparities in OS cells may stem from variations in the abundance levels of these essential metabolites.





# **The SCLIMS-identified protective metabolites promote healthy aging and extend lifespan**

The effect of key metabolites treatment across two different cell types confirmed the regulatory role of metabolism in OS and senescence, leading to the question whether key metabolites further regulate animal aging. To explore the regulatory effects of metabolism on animals, we introduced the *C. elegans* aging model<sup>60,61</sup> to investigate the impact

of the key metabolites (hypotaurine, phosphocreatine, and O-phosphoethanolamine) on the process of natural aging (Fig. 8a). A series of concentrations of the three metabolites were added into the Nematode Growth Medium (NGM) at the age of L4 and throughout the lifespan of the worms. The OS level, lifespan and healthspan of the worms were then evaluated. Strikingly, the supplement of hypotaurine, phosphocreatine and O-phosphoethanolamine at various doses



**Fig. 6 | Role of intracellular metabolic features in determining the cellular fate in OS and OS induced senescence.** **a** A flowchart showing the process of the analysis. The initial cells were clustered based on their metabolomic features with unsupervised clustering, revealing Cluster-I (blue palette) and Cluster-II (red palette). Then cells with top (blue strip) and bottom (red strip) 5%-50% GSH levels were projected to the UMAP scatter plot. The correct matches were defined as cells with top 5%-50% GSH levels to Cluster-I (blue dots), and cells with bottom 5%-50% GSH levels to Cluster-II (red dots). Incorrect matches were labeled as green dots. Finally, the fraction of correct matches was calculated. **b–f**, The visualization of projection of cells with top/bottom 5% (**b**), 15% (**c**), 25% (**d**), 35% (**e**), and 50% (**f**) GSH levels into Cluster-I and Cluster-II. Correct matches were labeled as blue (cells with top 5–50% GSH levels vs Cluster-I) and red (cells with bottom 5–50% GSH levels vs Cluster-II) dots. Incorrect matches were labeled as green dots. Cells with intermediate GSH levels were labeled as gray dots. **g** Quantification of fraction of accurate matches between cells with top/bottom 5%-50% GSH levels and Cluster-I and Cluster-II. Blue: correct matches; green: incorrect matches. **h**, Experimental setup of FACS

separation of MROR and MROS cells and gating of the FACS: cells with top 5% (MROR, blue) and bottom 5% (MROS, red) GSH intensity were collected according to their fluorescent intensity. **i, j** Representative images (**i**) and quantification (**j**) of DCFDA staining of MROR and MROS cells before and after OS induction.  $F(1, 8) = 7.405$ ,  $P = 0.0262$  in two-way ANOVA. **k, l** Representative images (**k**) and quantification (**l**) of SA- $\beta$ -Gal staining of MROR and MROS cells before and after induction of OS-induced senescence.  $F(1, 8) = 9.177$ ,  $P = 0.0163$  in two-way ANOVA. Scale bar, 50  $\mu\text{m}$ .  $P$  values in two-way ANOVA with Turkey's multiple comparisons were labeled in the plot.  $n = 3$  for each group. All  $P$  values were reported as multiplicity adjusted  $P$  values for multiple comparisons. Data was normalized to the values of MROR group in control cells. Data is presented as mean  $\pm$  s.e.m. For (**j, l**), Source data are provided as Source Data files. Blue: MROR cells; red: MROS cells. OS: oxidative stress. MROR cells: initial cells exhibiting a metabolome resembling that of OS-resistant cells. MROS cells: initial cells exhibiting a metabolome resembling that of OS-sensitive cells.

caused a remarkable extension in the lifespan of *C. elegans* by approximately 33%-50% (Fig. 8b and Supplementary Fig. 16a).

The OS level of the aged *C. elegans* were assessed by dihydroethidium (DHE) staining<sup>62</sup>. The findings unveiled a remarkable elevation in OS levels among aged worms, as indicated by the intensity of DHE. However, this surge in OS was mitigated upon supplementation with the three metabolites in *C. elegans* (Fig. 8c, d). The intensity of DHE was reduced by an average of 16% in metabolite treated worms.

It has been reported that the mobility of worms is drastically compromised in aging as a sign of deterioration of health<sup>63</sup>. We next examined the locomotion of worms treated with and without these metabolites from the L4 stage onwards. Aged nematodes (Day 9) were subjected to the “thrashing” assay, wherein their swimming movements were observed to assess their physical mobility<sup>63</sup>. The elderly worms exhibited a 43% decline in their thrashing rate, which was effectively ameliorated by the administration of hypotaurine, phosphocreatine and O-phosphoethanolamine (Fig. 8e, f and Supplementary Fig. 16b).

Another indication of the deterioration in health of aged *C. elegans* is the reduction in their speed of movement<sup>64</sup>. The worms at three different ages were analyzed and a progressively decline in free moving speed was indeed observed (Fig. 8g, h). The supplementation of the three metabolites from L4 improved the free moving speed of the aged worms (Fig. 8h and Supplementary Fig. 16c, d). Free moving speed of metabolite-treated worms was 1.4–1.8 fold higher compared with vehicle-treated worms at Day 9, and 1.1–1.2 fold higher at Day 5.

Thus, the key metabolites identified by SCLIMS, including hypotaurine, phosphocreatine, and O-phosphoethanolamine, possess remarkable potential to prolong lifespan and foster graceful aging in *C. elegans* by effectively preventing cellular OS and senescence.

## Discussion

Emerging evidence indicates a diversity of cellular subtypes in senescence<sup>7,8,65,66</sup>, cancer<sup>6,67</sup>, diabetes<sup>68,69</sup>, and inflammatory diseases<sup>70</sup>, suggesting that there is vast heterogeneity among cells in various biological processes. However, previous studies on cellular metabolism have predominantly been performed at the homogenate level, potentially disregarding the metabolic heterogeneity and intricate metabolic changes of individual cells. Due to the challenges in obtaining metabolomic information from individual live cells, determining metabolic heterogeneity in single cells has proven to be a formidable task. The SCMS technique we have previously established excels at unraveling the metabolome at a single-cell resolution<sup>17,18</sup>. However, it encounters challenges when it comes to correlating the single-cell metabolome with cellular function and phenotype. Recently, the integrative analysis across multiple modalities brought new insights into cellular heterogeneity and elucidated the underlying

mechanisms governing biological processes<sup>11,71–74</sup>, thereby illustrating the crucial role of cross-modality analysis. In this study, we established an approach called SCLIMS by combining SCMS and live-cell imaging to the metabolome of individual cells with their cellular OS status, thereby enabling a cross-modality analysis of both metabolomics profiles and cellular phenotypes at single-cell resolution. This technology provides some notable contributions. Firstly, with SCLIMS we unveiled distinct metabolic signatures among the six subtypes of cells under OS, each with specific oxidative levels. The detailed single-cell metabolic profile of OS has been dissected, revealing the deterioration of metabolic processes associated with redox balance, energy metabolism, lipid metabolism and mitochondrial function. The SCLIMS has not only confirmed various alterations in metabolism under OS as reported in previous studies, but also unveiled discoveries of metabolic changes, including modifications in amino acid metabolism and the transition from the “Malate-Aspartate Shuttle” to the more sophisticated “Glycerol Phosphate Shuttle”. Secondly, the utilization of machine learning analysis on the single-cell metabolome substantiates the predictive capacity of individual metabolic characteristics regarding cellular heterogeneity and phenotype. Thirdly, the SCLIMS has led to the discovery that the ultimate destiny of cells following OS induction is determined by their initial heterogeneity in metabolomics. Lastly, the key metabolites identified by SCLIMS exhibit protective effects against OS, cellular senescence, and natural aging. Overall, the SCLIMS technique sheds lights into the study of metabolic changes in OS and therapeutic interventions in aging.

In the present study, the SCLIMS shows that the heterogeneous states of cells can be predicted directly with their intracellular metabolome, showing a tight link between metabolic features and cellular phenotype. In addition, a more remarkable discovery revealed by the SCLIMS is that the destiny of cells under OS can be determined by their initial metabolomics status. This technology has verified that GSH is strongly correlated with many metabolites in the metabolome and may play a key role in cell fate determination, as evidenced by the fact that GSH-rich cells exhibit greater resistance to OS. However, it should be noted that such resistance is not solely attributed to GSH; rather, our SCLIMS analysis reveals elevated levels of other key metabolites such as hypotaurine, and O-phosphoethanolamine in cells exhibiting enhanced oxidative resistance. Indeed, the anti-oxidant effect of these metabolites has been further confirmed in the aged *C. elegans*. In essence, the GSH-cored metabolome serves as the determinant of cell phenotype and fate in OS. Among the top 15 rewired metabolites, GSH is well correlated with the other 13 metabolites including glutamate, creatine, glutamine, taurine, threonine, N-acetyl-aspartic acid, aspartic acid, asparagine, UDP-N-acetylglucosamine, proline, GABA, cystathionine, and glucose. These metabolites participate amino acids metabolism as well as carbohydrate metabolism, which were compromised in cells with higher OS levels (Fig. 3e). Other studies reported the

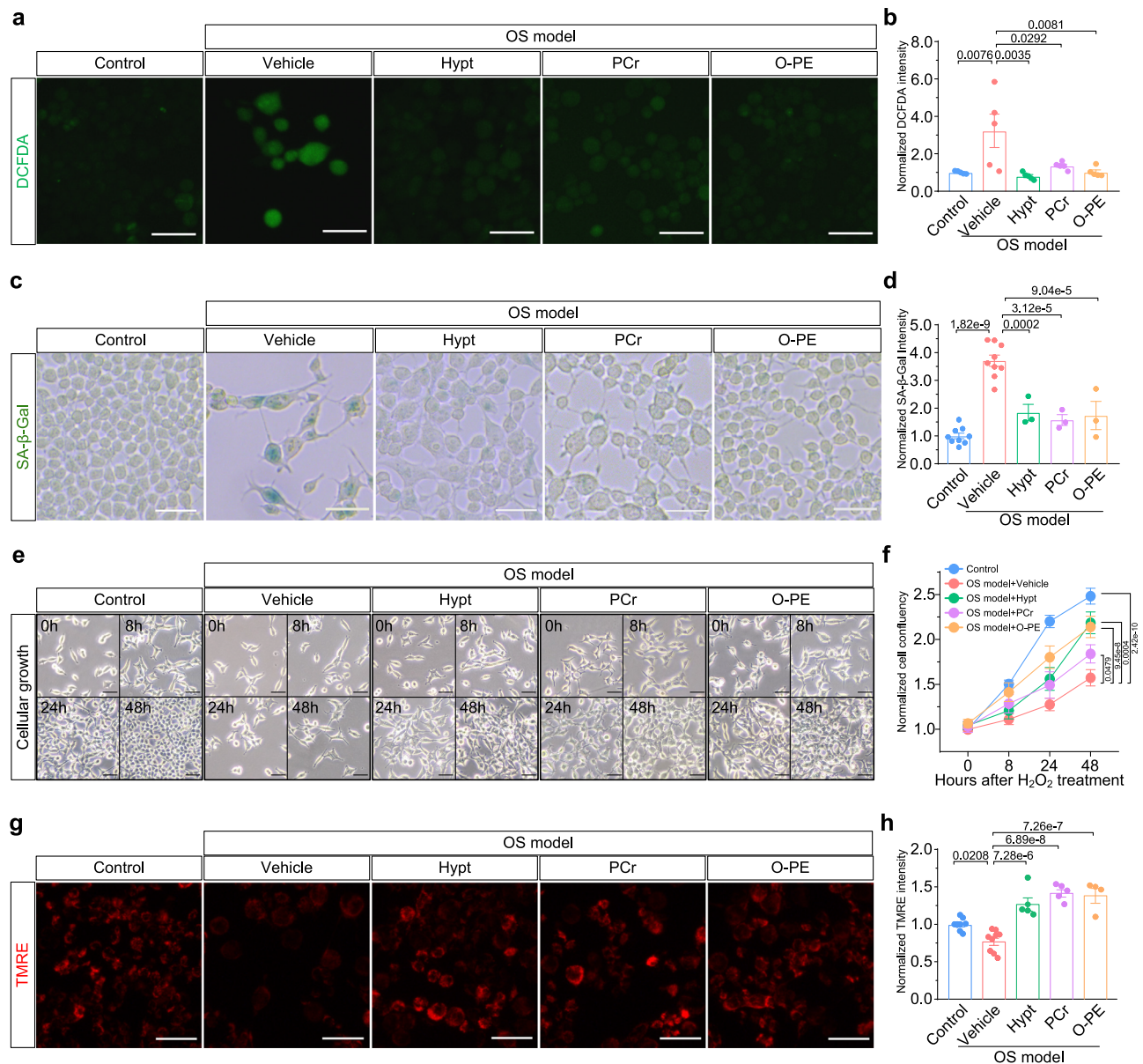


**Fig. 7 | Effects of key metabolites on OS and induced senescence.**

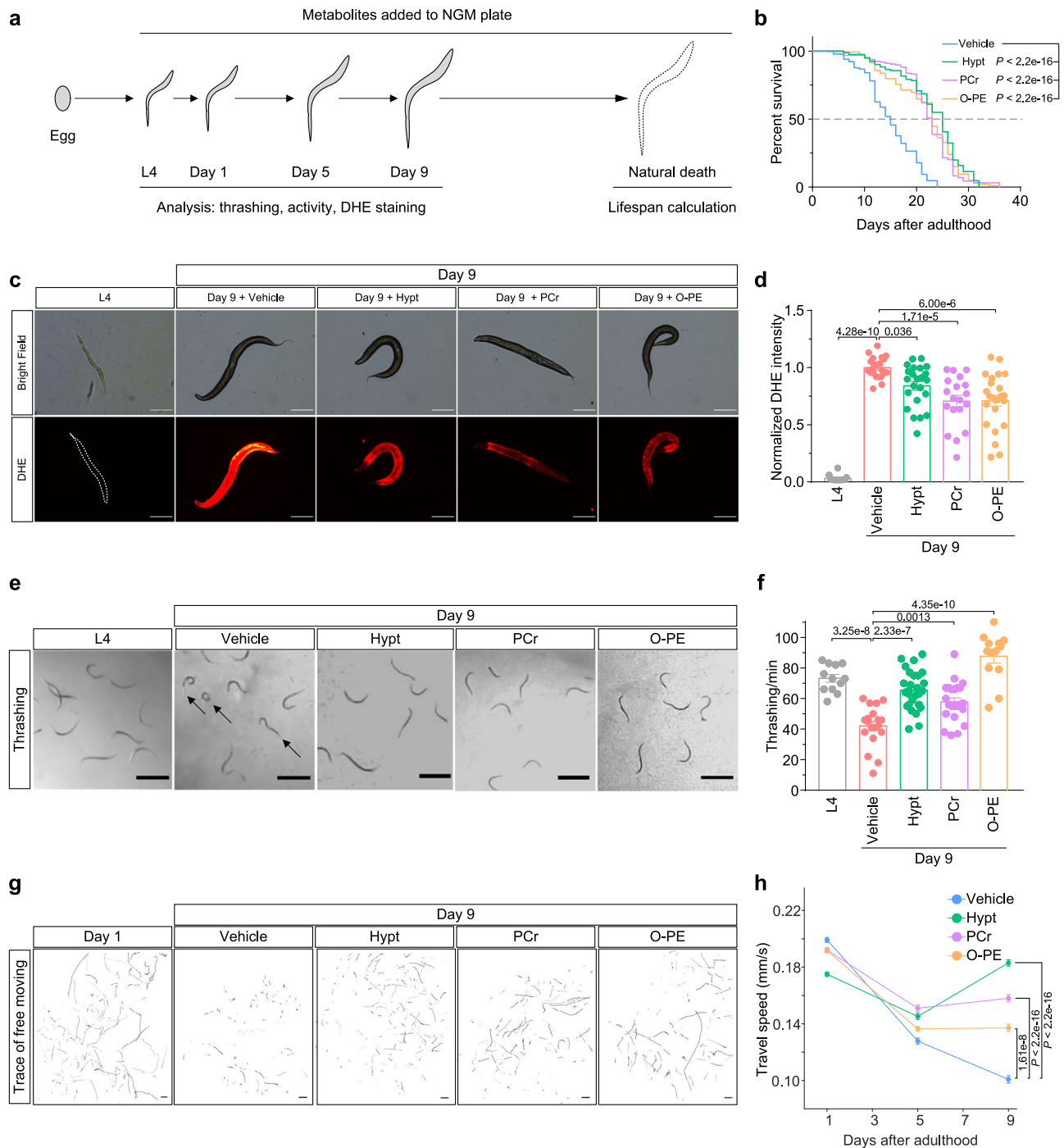
**a, b** Representative images (**a**) and quantification (**b**) of DCFDA staining of control cells and oxidative stressed cells with indicated treatments.  $n = 5$  for each group. Scale bar, 50  $\mu$ m.  $F(4, 20) = 5.991$ ,  $P = 0.0024$  in One-way ANOVA.  $P$  values in one-way ANOVA with multiple comparison were labeled in the plot. Data was normalized to values of control group. **c, d** Representative images (**c**) and quantification (**d**) of SA- $\beta$ -Gal staining of control and oxidative stressed cells with indicated treatments.  $n = 9, 9, 3, 3$ , and 3 for Control, Vehicle treated, Hypt treated, PCr treated, and O-PE treated group respectively. Scale bar, 50  $\mu$ m.  $F(4, 22) = 17.29$ ,  $P = 5.50e-9$  in One-way ANOVA.  $P$  values in one-way ANOVA with multiple comparison were labeled in the plot. Data were normalized to values of control group. **e, f** Representative images (**e**) and growth curve (**f**) of control and oxidative stressed cells with indicated treatments at indicated time points. Growth curve was plotted with at least 15 random fields from 3 independent biological replicates for each group at each indicated time point. Scale bar, 50  $\mu$ m.  $F(4, 520) = 41.26$ ,  $P < 2.2e-16$

in two-way ANOVA.  $P$  values in two-way ANOVA with Turkey's HSD comparison were labeled in the plot. Each group was compared with vehicle-treated oxidative stressed cells. Data were normalized to values of control group at 0 h.

**g, h** Representative images (**g**) and quantification (**h**) of TMRE staining of control and oxidative stressed cells with indicated treatments.  $n = 9, 9, 5, 5$ , and 4 for Control, Vehicle treated, Hypt treated, PCr treated, and O-PE treated group respectively. Scale bar, 50  $\mu$ m.  $F(4, 27) = 26.12$ ,  $P = 6.14e-9$  in one-way ANOVA.  $P$  values in one-way ANOVA with multiple comparison were labeled in the plot. Data was normalized to values of control group. All data are presented as mean  $\pm$  s.e.m. OS: oxidative stressed cells; Hypt: hypotaurine (1 mM); PCr: phosphocreatine (0.5 mM); O-PE: O-phosphoethanolamine (40  $\mu$ M). All  $P$  values were reported as multiplicity adjusted  $P$  values for multiple comparisons. For (**b, d, f, h**), Source data are provided as Source Data files. Blue: control; red: OS+vehicle; green: OS+Hypt; purple: OS+PCr; yellow: OS+O-PE.

effects of these top-rewired metabolites in aging and senescence as well. For example, taurine was reported to decline in aging and supplement of taurine increases healthspan and lifespan in various species<sup>75</sup>. Taurine protected telomerase and mitochondrial function, along with decreasing inflammation and DNA damage. Creatine was reported to promote healthy aging by attenuating inflammation and

preventing bone mineral loss<sup>76</sup>. Creatine improved neuronal function by antioxidant effect and exhibited therapeutic effect against age-related diseases including Alzheimer's disease, Parkinson's disease, and heart failure<sup>77</sup>. The level of threonine, aspartic acid, and proline were reported to be positively correlated with lifespan of yeasts<sup>78</sup>. Glutamine promotes autophagy via AMPK $\alpha$  lactylation and suppresses



senescence<sup>79</sup>. N-acetyl-aspartic acid was reported to decline in aging and was related to brain atrophy<sup>80</sup>. Asparagine prevented stem cell aging by regulating the autophagy-lysosome pathway<sup>81</sup>. The underlying mechanism behind the notable disparity in metabolic characteristics among initial cells remains elusive and necessitates further investigations. However, a possible explanation is that it could be a result of the asymmetric division of cytoplasm during cell division<sup>82–85</sup>. Another possibility may be attributed to differences in cellular contact, micro-environmental development, or potential transport of certain metabolites between neighboring cells that has gone undetected<sup>86</sup>. However, from a metabolic view, abundance of key metabolites determined the metabolomic profile of cells and recovered the disrupted metabolic pathways and the metabolome under OS along with reducing the OS and senescent level (Fig. 7 and

Supplementary Figs. 14, 15), suggesting the role of key metabolites in determining the metabolic and phenotypic heterogeneity.

The SCLIMS-identified key metabolites provides opportunities in senescence and aging intervention. The OS-induced senescence is one of the important models of cellular senescence<sup>22,54,55</sup> and play crucial role in various diseases<sup>87,88</sup>. The supplementation of the key metabolites, including hypotaurine, phosphocreatine, and O-phosphoethanolamine, can effectively mitigate the cellular OS and the OS-induced senescence. Moreover, these metabolites also prevent OS, prolong lifespan, promote healthy aging and delay the decline in mobility during aging in *C. elegans*. Combining the clues from the literature, we posit that these metabolites may regulate cellular OS and senescence through multiple mechanisms. For instance, hypotaurine serves as a hydrogen donor for NAD<sup>+</sup> during its conversion into taurine, thereby



**Fig. 8 | Metabolic intervention extends lifespan and promotes healthy aging in *C. elegans*.** **a** A flowchart of experimental setup of lifespan and healthspan assay of *C. elegans*. **b** Lifespan of *C. elegans* treated with vehicle ( $n = 221$ ), 0.4 mM hypotaurine (Hypt) ( $n = 320$ ), 0.2 mM phosphocreatine (PCr) ( $n = 225$ ) and 0.1 mM O-Phosphoethanolamine (O-PE) ( $n = 387$ ).  $P$  values in two-tailed log rank test compared with vehicle-treated worms were labeled in the plot,  $P < 2.2 \times 10^{-16}$  for all comparisons indicated in (b). **c, d** Representative images (c) and quantification (d) of DHE staining of L4 (young adult) ( $n = 14$ ) and Day-9 (aged) worms with indicated treatments ( $n = 21, 23, 19$ , and  $24$  for vehicle, Hypt, PCr, and O-PE treated worms respectively). Scale bar, 200  $\mu\text{m}$ .  $F(4, 96) = 65.74$ ,  $P < 2.2 \times 10^{-16}$  in One-way ANOVA.  $P$  values in One-way ANOVA with multiple comparison were labeled in the plot.  $P$  values were reported as multiplicity adjusted  $P$  values for multiple comparisons. Data was normalized to values of vehicle treated group at Day 9. Data is presented as mean  $\pm$  s.e.m. **e, f** Representative images (e) and quantification (f) of L4 ( $n = 12$ ) and aged *C. elegans* thrashing under treatment of vehicle ( $n = 19$ ), 0.4 mM hypotaurine (Hypt) ( $n = 28$ ), 0.2 mM phosphocreatine (PCr) ( $n = 23$ ) and 0.1 mM O-Phosphoethanolamine (O-PE) ( $n = 13$ ). Arrows indicate immobilized worms. Scale bar, 1 mm.  $F(4, 90) = 27.58$ ,  $P = 6.00 \times 10^{-15}$  in One-way ANOVA.  $P$  values in One-way ANOVA with multiple comparison were labeled in the plot.  $P$  values were reported

as multiplicity adjusted  $P$  values for multiple comparisons. **g, h** Representative traces (g) and quantification (h) of free moving *C. elegans*. The traces showed the track of free moving worms in 1 min. At day 1, data of tracks was derived from 294, 368, 317, and 391 worms for vehicle, Hypt treated, PCr treated, and O-PE treated group, respectively. At day 5, data of tracks was derived from 184, 284, 175, and 305 worms for vehicle, Hypt treated, PCr treated, and O-PE treated group, respectively. At day 9, data of tracks was derived from 176, 309, 316, and 153 worms for vehicle, Hypt treated, PCr treated, and O-PE treated group, respectively. Scale bar, 1 mm.  $F(3, 26296) = 73.15$ ,  $P = 4.17 \times 10^{-47}$  in Two-way ANOVA.  $P$  values in Two-way ANOVA with Turkey's HSD comparison (vehicle vs O-PE, Hypt, and PCr, respectively) were labeled in the plot.  $P$  values were reported as multiplicity adjusted  $P$  values for multiple comparisons. Data were collected from 3 independent biological replicates. For (b, d, f, h), Source data are provided as Source Data files. For (b and h), blue: Vehicle treated worms; green: Hypt treated worms; purple: PCr treated worms; yellow: O-PE treated worms. For d and f, gray: L4 worms; red: vehicle treated aged worms; green: Hypt treated aged worms; purple: PCr treated aged worms; yellow: O-PE treated aged worms. Hypt: 0.4 mM hypotaurine; PCr: 0.2 mM phosphocreatine; O-PE: 0.1 mM O-Phosphoethanolamine.

generating NADH as a by-product<sup>31</sup>. This process effectively restores redox balance in the presence of OS. Phosphocreatine serves as a direct catalyst for the conversion of ADP into ATP<sup>89</sup>, functioning as a quintessential cellular energy reservoir that possesses the inherent capability to reinstate equilibrium in energy levels. O-phosphoethanolamine has been reported to mitigate mitochondrial dysfunction<sup>90</sup> and effectively restore membrane, as it serves as the fundamental precursor of membrane lipids<sup>91</sup>. Therefore, these metabolites may potentially impede senescence by modulating various cellular processes, including energy metabolism, mitochondrial function, and lipid metabolism. The deficiency of such metabolites may render cells more susceptible to senescence-inducing factors, such as OS. Furthermore, a more paramount consequence of the metabolic intervention lies in its ability to prolong healthspan, which assumes a relatively pivotal role in the realm of aging research when compared to lifespan<sup>63,92</sup>. The decline of physical function is a common occurrence in both the early and late stages of aging, and bestowing longevity upon frailty offers minimal advantage to the individual<sup>93</sup>. Therefore, screening for potential metabolites from our SCLIMS database presents an opportunity for promoting health benefits during the aging process.

The current study has certain limitations that we would like to address, along with potential solutions for future studies. Firstly, the identification of metabolites at the single-cell level poses a significant challenge due to the complexity of MS/MS analysis. Acquiring MS/MS spectra for hundreds of  $m/z$  in the metabolome is indeed arduous. However, there are promising avenues to enhance metabolite identification efficacy. For instance, ion mobility mass spectrometry can potentially differentiate metabolites sharing identical  $m/z$  values by considering collision cross section<sup>94–96</sup>. Additionally, optimizing scan speed and extending sampling duration can facilitate acquiring comprehensive MS/MS spectra from single cells<sup>97</sup>. Secondly, the SCLIMS utilized in this current study was meticulously designed to incorporate cultured cells and cellular models of OS. The versatility of SCLIMS extends to tissue-embedded cells, as they can also be effectively labeled with fluorescence markers. However, the potential application of SCLIMS in tissue-embedded cells remains an intriguing area for future exploration and investigation. Thirdly, one must acknowledge the challenges associated with analyzing fixed cells when employing the SCLIMS technique. Nevertheless, by enabling analysis of fixed cells, a myriad of phenotypic features such as SA- $\beta$ -Gal staining, immunofluorescence analysis, and immunohistochemistry can be seamlessly integrated into the cell metabolome profiling process.

In summary, this study presents a cross-modality analysis integrating single-cell metabolomic profile and cellular phenotype enhancing our understanding of cell heterogeneity and subtype-

specific metabolic signatures in a cellular model of OS. Most importantly, the cross-modality platform and analysis described in this study provide a way in single-cell research. The single-cell metabolome and the cellular phenotype such as OS status are directly linked and integrated. The heterogeneous states are explained with single-cell metabolome and metabolic pathways. Significantly, the insights into the metabolic regulation governing OS, cellular senescence, and natural aging serves as a valuable resource for future investigations into interventions targeting oxidative damage, aging and senescence. Furthermore, this cutting-edge platform possesses the remarkable capability to integrate single-cell metabolomics profiling with a diverse array of cellular phenotypes assessed by live-cell labeling. For instance, (1) The SCLIMS can be combined with live-cell mitochondrial probes such as probes for mitochondrial membrane potential (i.e. TMRE probe) and mitochondrial morphology (i.e. Mito-Tracker). This enables the study of the interaction between mitochondrial function and the metabolome at single-cell level; (2) The SCLIMS can be integrated with calcium imaging<sup>98</sup> which labels neuronal activities and enables the performance of multi-modal analysis of heterogeneity in metabolome and neuronal functions; (3) The SCLIMS can be utilized to investigate the correlation between cellular metabolome and cell cycle by incorporating dynamic live-cell fluorescent probes for real-time monitoring of cell division and proliferation<sup>99</sup>. Thus, with any technique labeling live cells with fluorescent, this cross-modality platform will become a feasible way for integrative analysis and a powerful tool for the discovery of secrets in single cells.

## Methods

### Chemicals

NaCl, KCl,  $\text{CaCl}_2$ ,  $\text{MgCl}_2$ , HEPES, NaOH, sucrose,  $\text{NH}_4\text{HCO}_3$ ,  $\text{Na}_2\text{HPO}_4$ ,  $\text{KH}_2\text{PO}_4$ ,  $\text{K}_2\text{HPO}_4$ ,  $\text{MgSO}_4$ , cholesterol, hypotaurine, and O-phosphoethanolamine were purchased from Sigma-Aldrich. Phosphate buffer saline was purchased from Sangon Biotech. Dulbecco's Modified Eagle's medium (DMEM) was purchased from HyClone. Fetal bovine serum and trypsin-EDTA (0.25%) were purchased from Gibco. Trypan blue, penicillin and streptomycin were purchased from Biosharp. Hydrogen peroxide was purchased from Sinopharm. Phosphocreatine was purchased from Aladdin. The Senescence-Associated  $\beta$ -Galactosidase kit and Mitochondrial membrane potential assay kit were purchased from Beyotime. A cellular ROS assay kit and dihydroethidium (DHE) were purchased from Abcam. Live-cell GSH probe (mCIB) was purchased from MedChemExpress.

### Cell culture

HEK293T cell line were originally obtained from ATCC (CRL-3216). The cell line was authenticated by ATCC with STR profiling. Primary MEFs



were a kind gift from Professor Chunlei Cang in University of Science and Technology of China. All cells were cultured in Dulbecco's Modified Eagle's medium (DMEM) (HyClone), supplemented with 10% fetal bovine serum (FBS, Gibco) and 100 U/ml penicillin 100 µg/ml streptomycin (Biosharp) at a temperature of 37 °C, with 5% CO<sub>2</sub> in a humidified atmosphere. The culture medium was refreshed every 2–3 days, and the cells were subcultured every 3–5 days when they reached approximately 80% confluency.

### ***C. elegans* strain and maintenance**

The *Caenorhabditis elegans* (*C. elegans*) were cultured and maintained on Nematode Growth Medium (NGM) seeded with *E. Coli* OP50 at 20 °C. N2 (wild isolate) strain was used in all *C. elegans* experiments. Plates were maintained by transferring the worms every 3 days. For DHE staining and thrashing analysis, worms at L4 and at Day 9 after L4 were used. For lifespan analysis, the survival of worms was observed throughout the whole lifespan. For activity analysis, worms at Day 1, Day 5 and Day 9 after L4 were used.

### **Oxidative stress model**

Cells were seeded and allowed to grow overnight. Subsequently, they were treated with hydrogen peroxide at a final concentration of 80 µM for HEK293T cells and 240 µM for MEFs in the culture medium for 1 h, followed by replacement with fresh medium. Finally, the cells were cultured for an additional 48 h to establish an oxidative stress model.

### **Treatment of cells with metabolites**

Cells were seeded and allowed to grow overnight. Subsequently, the cells were treated with hydrogen peroxide at a final concentration of 80 µM for HEK293T cells and 240 µM for MEFs in culture medium for 1 h. After that, the medium was replaced with fresh medium supplemented with specific metabolites at indicated concentrations. The cells were then cultured for an additional 48 h before further assays.

### **Metabolite treatment and life span assay of *C. elegans***

Life span assays of *C. elegans* were conducted at a temperature of 20 °C. Metabolite treatment was administered by adding specific metabolites at the indicated concentrations to NGM plates, which were then incubated overnight prior to use. Following bleaching, age-synchronized eggs were washed with M9 buffer and subsequently placed on NGM plates. Late L4 larvae or young adult worms were subsequently transferred to NGM plates that had been seeded with heat-inactivated OP50 *E. coli* and supplemented with 0.1 mg/ml of 5'-FUDR, as well as the indicated treatment of metabolites. Approximately 100 worms were placed on each plate, which was then inspected and scored every one to two days. The worms were moved to fresh plates every one to two days in order to ensure the efficacy of the drugs and metabolites. Worms that exhibited no response to mechanical stimulation were considered deceased. Worms displaying a "protruding vulva", those that were lost, or had burrowed into the medium were censored. Statistical analysis was conducted using the MATLAB function "logrank" ([www.mathworks.com/matlabcentral/fileexchange/22317](http://www.mathworks.com/matlabcentral/fileexchange/22317)), and *P* values were calculated.

### **Behavioral analysis of *C. elegans***

The 'thrashing' assay was employed to assess the locomotion of *C. elegans*. On Day 9 post-adulthood, worms subjected to specific treatments were transferred to M9 buffer and allowed to acclimate for 1 min before body bends were quantified using a dissecting microscope.

The physical function of *C. elegans* was assessed by monitoring the locomotion of the worms on NGM plates. On Day 1, Day 5, and Day 9 post-adulthood, freely moving worms subjected to specific treatments were recorded using a digital camera and analyzed in ImageJ (version 1.54 g, <https://imagej.nih.gov/ij/>) with the 'wrMTrack' plugin as

per manual instructions. The traveling speed was then calculated using the plugin.

### **Cell viability assay**

Cell viability assay was performed according to the manufacturer's manual. Cells were dissociated using trypsin-EDTA (0.25%) (Gibco) for 1 min at 37 °C, followed by termination of the dissociation process through the addition of an equal volume of DMEM supplemented with 10% fetal bovine serum. Cells were suspended, centrifuged, and then resuspended with PBS. Subsequently, they were stained with trypan blue (Biosharp) at a final concentration of 0.04%. The cells were then enumerated under a microscope; the stained cells were designated as non-viable. Cell viability was determined by calculating the ratio of unstained cells to the total number of both stained and unstained cells.

### **SA-β-Gal assay**

The experimental procedure was performed in accordance with the protocols provided by the SA-β-Gal assay kit (Beyotime, China). Briefly, cells were washed with phosphate-buffered saline (PBS) and fixed with fixing reagents at room temperature for 15 min. After three washes with PBS for 3 min each, staining solution was prepared according to the manufacturer's instructions prior to use. Cells were stained overnight at 37 °C, and images of five randomly selected fields were captured using a bright field setting for subsequent analysis.

### **Oxidative stress assay**

To evaluate the extent of cellular oxidative stress, a live-cell probe DCFDA was prepared according to the manufacturer's protocol (Abcam). Subsequently, live cells were incubated with a 10 µM DCFDA solution for 25 min at 37 °C and 5% CO<sub>2</sub>, followed by PBS washing. Images were promptly captured using a fluorescent microscope (Leica), and five random fields were selected for analysis in each dish.

To assess the level of oxidative stress in *C. elegans*, worms were exposed to a final concentration of 3 µM DHE (Dihydroethidium) in M9 buffer at 20 °C for 30 min, followed by washing with M9 buffer. Subsequently, the worms were transferred onto glass slides and imaged using a fluorescent microscope (Leica).

### **Mitochondrial membrane potential assay**

TMRE was utilized to assess the mitochondrial membrane potential (MMP) of viable cells in accordance with the manufacturer's instructions. Briefly, cells were incubated with 1X TMRE (Beyotime) in serum-free DMEM for 15 min at 37 °C. Subsequently, the cells were rinsed with warm serum-free DMEM and immediately imaged using a fluorescent microscope (Leica, version 4.6.2 build: 410). Images of five randomly selected fields were captured for analysis.

### **Analysis of SA-β-Gal intensity**

The SA-β-Gal-stained area in images of random fields was extracted using the 'IHC toolbox' plugin in ImageJ, resulting in a new image of the stained area. The color images of the extracted SA-β-Gal stained area were then converted to 8-bit grayscale and calibrated within ImageJ (version 1.54g). Finally, the gray value (integrated density) of the stained area was calculated using ImageJ. The intensity of SA-β-Gal was quantified by calculating the gray value (integrated density) of the stained area normalized to the total cell area in each image.

### **Analysis of fluorescence intensity**

For random field images, color images of cells stained with fluorescent live-cell probes (DCFDA and TMRE) were imported into ImageJ software. The images were then converted to 8-bit grayscale and calibrated before being thresholded. The fluorescence intensity was calculated as the mean gray value of cells in the field by measuring the integrated density of fluorescent positive area divided by the fluorescent positive area. For single cells, the image was converted to an 8-bit grayscale

image and calibrated. Fluorescent intensity was analyzed using ROI manager in ImageJ, which allowed for analysis of individual cells through selection. The mean gray value for each cell was calculated by dividing the integrated density of a cell by its area.

For *C. elegans*, the level of oxidative stress (indicated by DHE fluorescence) was quantified using ImageJ software. The color images were converted to 8-bit grayscale and calibrated prior to thresholding. The gray value (integrated density) of fluorescent positive areas in individual worms was then calculated and normalized by the corresponding area.

### The workflow and experimental setting of SCLIMS

The SCLIMS platform comprises two primary components: live-cell imaging and single-cell MS. Cells were initially stained with a 10  $\mu$ M DCFDA solution for 25 min at 37 °C and 5% CO<sub>2</sub>, followed by PBS washing. Subsequently, the cells were captured using a fluorescent microscope to record their spatial distribution. The acquired images were subsequently subjected to analysis, enabling the calculation of oxidative stress levels in individual cells.

The cells were then transferred to the single-cell patch clamp platform and incubated in a bath solution containing 140 mM NaCl, 5 mM KCl, 2 mM CaCl<sub>2</sub>, 1 mM MgCl<sub>2</sub> and 10 mM HEPES (pH adjusted to 7.4 with NaOH; ~320 mosmol with sucrose) and approached by a borosilicate glass pipette filled with pipette solution (88 mM NH<sub>4</sub>HCO<sub>3</sub>) using a micromanipulator. The cells were selected based on the fluorescent images acquired in the preceding step. The cells were patched with a high-quality seal (>1 G $\Omega$ ) and the cell membrane was disrupted by rapid application of negative pressure. Mild negative pressure was then applied to the pipette to obtain cytoplasmic chemical constituents, which were subsequently analyzed using mass spectrometry after removal of the pipette from the bath solution.

Following the extraction of cellular cytoplasmic constituents, the capillary was connected to a MS system as described below. An AC voltage of 4 kV amplitude and approximately 500 Hz frequency was applied externally to the spray capillary micropipette, while maintaining a distance of approximately 5 mm between the tip of the spray micropipette and the orifice of the MS instrument. High-resolution mass measurements were analyzed using a Q Exactive Plus MS instrument (Thermo Fisher Scientific, San Jose, CA, USA). nanoESI source and Orbitrap mass analyzer were used. The main experimental parameters were established as follows: capillary temperature at 275 °C, S-lens radio frequency (RF) level set to 50%, mass resolution of 70,000, maximum injection time of 10 ms, AGC target of 1e6, and microscan rate of 1. Negative ion mode was employed throughout all experiments. Data was acquired under full scan mode. For MS/MS, collision energy was set to hcd = 30. Data was collected with Thermo Scientific Exactive Tune software (version 2.9.0.2926). The MS data were then processed. Data of each single cell was paired with oxidative stress levels based on the fluorescent images.

### Single-cell mass spectrometry data processing

The spectral data of individual cells were initially stored in separate files by the instrument. Subsequently, all files were converted into mzML format using ProteoWizard (version 3.0.9870). The XCMS package (version 3.9.1) in R statistical environment was utilized to process all single-cell MS data, encompassing peak calling, peak alignment, and quality control. A signal-to-noise (S/N) filter of 3 was applied to the m/z signal, and metabolic signals were identified as those with a frequency exceeding 20% across all tested cells. The data was organized into a matrix, where metabolites were represented by rows and cells were represented by columns. All intensities were normalized to the total ion current (TIC) ratio. Metabolites were annotated by comparing observed m/z values with theoretical values in the Human Metabolome Database v5.0 ([www.hmdb.ca](http://www.hmdb.ca)), and m/z

annotations were assigned if errors fell within 10 ppm. To ensure the precision of the annotations, metabolites underwent further identification employing MS/MS. For metabolites involved in treating OS cells and worms including hypotaurine, phosphocreatine, and O-phosphoethanolamine, their confirmation relied on matching MS/MS spectra between cells and standards (Supplementary Fig. 17). Other metabolites were identified by comparing MS/MS spectra between bulk cellular samples and the HMDB database. Batch effects of experiments were assessed through PCA and HCA analysis in the R statistical environment.

### Flow cytometry

The cells were seeded and cultured until they achieved a confluency of 70–80%. Following a single wash with 1 mL of phosphate-buffered saline (PBS), the cells were dissociated using 0.25% trypsin solution containing EDTA, after which the reaction was halted by supplementing DMEM with FBS at a concentration of 10%. Subsequently, the cell suspension was collected in tubes measuring approximately 1.5 mL capacity and subjected to centrifugation at a speed of 600  $\times$  g for 5 min before being resuspended in PBS containing mCIB at a final concentration of 40  $\mu$ M. The resuspended cells were then incubated at a temperature of precisely maintained at or around 37 °C for 20 min. Subsequently, the cells were washed and resuspended in PBS supplemented with 1% FBS. After filtration through a 40  $\mu$ m cell strainer and transfer to clean tubes, all samples were vortexed for 5 s to ensure complete dissociation into single-cell suspension prior to flow cytometry analysis. Flow cytometric analysis was performed using a BD FACSaria III instrument (BD Biosciences), with initial gating based on FSC-A versus SSC-A parameters followed by measurement of whole-cell fluorescence. Unstained cells were utilized as a blank control to establish baseline correction. Finally, cells stained with mCIB exhibiting the top and bottom 5% fluorescent intensity were isolated and collected independently for subsequent analysis. The FACS data was then analyzed and visualized using the 'fca\_readfcs' function and the 'Flow cytometry GUI for MATLAB' plugin in MATLAB (version 2022b) ([www.mathworks.com/matlabcentral/fileexchange/9608-fca\\_readfcs](http://www.mathworks.com/matlabcentral/fileexchange/9608-fca_readfcs) and [www.mathworks.com/matlabcentral/fileexchange/38080-flow-cytometry-gui-for-matlab](http://www.mathworks.com/matlabcentral/fileexchange/38080-flow-cytometry-gui-for-matlab)).

### Identification of marker metabolites

Wilcoxon rank-sum tests were used to compare metabolites in cells belonging to one cluster with those of all other cells, based on the results obtained from unsupervised clustering analysis. Ions exhibiting  $P < 0.05$  and fold change (FC) > 1.5 were identified as marker metabolites for the specific cluster, which were subsequently z score scaled and visualized using MATLAB's 'heatmap' function. The z score scales the data for each ion and is calculated as follows:

$$z = \frac{x - \bar{X}}{S} \quad (1)$$

where z represents z score, x represents a sample raw data,  $\bar{X}$  represents the population mean, and S represents the population standard deviation.

### Identification of metabolic subtypes

The metabolic data matrix was imported into the MATLAB workspace, where it underwent z score scaling and unsupervised clustering using the k-medoids algorithm. The resulting clusters were visualized with Uniform Manifold Approximation and Projection (UMAP) via a MATLAB plugin ([https://www.mathworks.com/matlabcentral/fileexchange/71902](http://www.mathworks.com/matlabcentral/fileexchange/71902)). The data was dimensionally reduced to two dimensions and subsequently visualized using the 'gscatter' function in MATLAB (version 2022b), revealing distinct metabolic subtypes of cells within a bi-dimensional space.

### Pseudotime analysis and single-cell trajectory construction

The metabolite data matrix was initially filtered based on the correlation with oxidative stress level (indicated by DCFDA intensity). Metabolites exhibiting a correlation coefficient ( $r$ ) greater than 0.2 or less than -0.2 and  $P < 0.05$  in correlation analysis were selected for pseudotime analysis. The refined data matrix was then imported into Monocle (version 2.16.0) in R statistical environment, followed by dimensional reduction using the 'DDRTree' algorithm according to the documentation of Monocle (<https://cole-trapnell-lab.github.io/monocle-release/>). Finally, the 'plot\_cell\_trajectory' function was utilized to visualize the trajectory.

### Supervised machine learning and model evaluation

Supervised machine learning was conducted using MATLAB (version 2022b). The data matrix was randomly divided into a training dataset and a testing dataset at a ratio of 2:1. The testing dataset was exclusively used for evaluating the trained model and not exposed to the training phase. The training of both the classification and regression models was conducted without any feature selection, and all m/z signals that met our criteria ( $S/N > 3$  and detected in greater than 20% single cells) were included in both the training and testing datasets. To train classification models, ensemble algorithm (function 'fitcensemble'), discriminant analysis algorithm (function 'fitcdiscr') and neural network algorithm (function 'fitnet') were employed as specified. The model underwent 5-fold cross-validation during training, with Bayesian optimization employed to optimize hyperparameters and minimize cross-validation loss (error). Parameters 'Method', 'NumLearningCycles', 'MinLeafSize', and 'LearnRate' were automatically optimized in the ensemble algorithm, while parameters 'Delta' and 'Gamma' were automatically optimized in the discriminant analysis algorithm. Parameters such as 'Activations', 'Lambda', 'LayerSizes', and 'Standardize' were automatically optimized for neural network algorithm. For the training of regression models, we utilized the neural network algorithm (function 'fitnet'). The data underwent a "log2" or "ln" transformation and was trained using 5-fold cross-validation and Bayesian optimization. Parameters such as 'Activations', 'Lambda', 'LayerSizes', and 'Standardize' were automatically optimized.

After training the model with the training dataset, the testing dataset was utilized to evaluate the performance of the classification models through receiver operating characteristic (ROC) curve and confusion matrix analysis. For multiclass problem, 'one versus rest' strategy was used which transformed the problem into a two-classification task. The predicted vs real scatter plot and the Pearson's  $r$  and  $P$  value were used to evaluate the performance of the regression model.

### Evaluation of metabolic similarity

The 'pdist' function in MATLAB (version 2022b) was utilized to compute the statistical distance based on the cellular metabolome, where a larger distance indicated a lower degree of similarity between two cells. Similarity was calculated as the reciprocal of distance. The heatmap was generated by plotting the reciprocal of the distance as a measure of similarity, with higher values indicating greater likelihood of shared metabolomic features between cells. We quantified the pairwise distances between cells in the initial and OS groups based on their metabolite abundance as variables. Spearman distance functions were employed.

Spearman distance function:

$$d_{s,t} = 1 - \frac{(r_s - \bar{r}_s)(r_t - \bar{r}_t)'}{\sqrt{(r_s - \bar{r}_s)(r_s - \bar{r}_s)'} \sqrt{(r_t - \bar{r}_t)(r_t - \bar{r}_t)'}} \quad (2)$$

where  $d_{s,t}$  represents the distance between two cells ( $s$  and  $t$ );  $r_{sj}$  is the rank of  $x_{sj}$  taken over  $x_{1j}, x_{2j}, \dots, x_{mj}$ ;  $r_s$  and  $r_t$  are the coordinate-wise rank vectors of  $x_s$  and  $x_t$ , as an example,  $r_s = (r_{s1}, r_{s2}, \dots, r_{sn})$ ;  $\bar{r}_s = \frac{1}{n} \sum_{i=1}^n r_{si}$  and  $\bar{r}_t = \frac{1}{n} \sum_{i=1}^n r_{ti}$ .  $n$  represents the number of variables.

Hamming distance was used in the comparison of metabolome of Hypt, PCr, O-PE treated OS cells with Non-OS and vehicle treated OS cells.

Hamming distance function:

$$d_{s,t} = \left( \frac{\#x_{sj} \neq x_{tj}}{n} \right) \quad (3)$$

where  $d_{s,t}$  represents the distance between two cells ( $s$  and  $t$ );  $x_{sj}$  represents the variable  $j$  of the first cell  $s$ ,  $x_{tj}$  represents the variable  $j$  of the second cell  $t$ ;  $n$  represents the number of variables. The function calculates the fraction of different variables in all variables ( $n$ ) of the two cells.

### Metabolite set enrichment analysis

Metabolite set enrichment analysis (MSEA) was performed using MetaboAnalyst (v6.0), an online metabolomics analysis tool ([www.metaboanalyst.ca](http://www.metaboanalyst.ca)). The annotation of metabolites, including metabolic markers in clusters and those correlated with the oxidative stress level of single cells, was compiled into a list and uploaded to the website. Only metabolites identified with MS/MS confirmation was used in the MSEA. The algorithm processed the data and obtained enriched pathways, while also calculating two important parameters: Enrichment Ratio and  $P$  value. Enrichment Ratio indicates the degree of enrichment, while  $P$  value represents its significance. Pathways with a  $P$  value less than 0.05 were deemed significant. The results were downloaded from the website and visualized using MATLAB's 'bubblechart' function.

### Construction of metabolic networks and rewiring analysis

The annotated metabolite data was analyzed using the 'corr' function in MATLAB (version 2022b), resulting in a matrix of correlation coefficients ( $r$ ). This matrix was then reorganized into three columns: metabolite-1, metabolite-2, and their respective correlation coefficient values. The reorganized matrix was imported into Cytoscape (version 3.10.1) to construct metabolic networks based on the correlations between metabolites. In analysis of Cluster-I and Cluster-II in initial cells, metabolite pairs with  $P > 0.05$  or  $|r| < 0.8$  were excluded. In the network, nodes represent metabolites, and edges represent correlations. The networks of correlation were visualized using Cytoscape. By utilizing the DyNet algorithm to compare two different networks, changes in relationships with other metabolites for each individual metabolite were analyzed. Metabolite rewiring scores were calculated using the DyNet algorithm and then visualized through stem plot with MATLAB's 'stem' function.

### Statistical analysis

The statistical analysis was conducted using Microsoft Excel (Microsoft), R statistical environment, MATLAB 2022b (Mathworks), and GraphPad Prism (version 8). The Wilcoxon rank sum test was employed to determine the significance of two-grouped data, while one-way ANOVA or two-way ANOVA were utilized for multi-group or multi-factor data, respectively. Distribution analysis (using the "Rayleigh" probability density function) and calculation of interquartile range (IQR) and median absolute deviation (MAD) were performed using MATLAB R2022b (MathWorks). Sample size was not predetermined by statistical methods in this study, but rather based on previous experience. The number of samples ( $n$ ) is indicated in the figures or figure legends.



## Reporting summary

Further information on research design is available in the Nature Portfolio Reporting Summary linked to this article.

## Data availability

The metabolomic data generated in this study have been deposited in the MassIVE database under accession code [MSV000097134](https://massive.ucsd.edu/MSV000097134). The metabolomic data are available under restricted access for the reason that the data is under further research and investigations, access can be obtained by sending a request explaining the aim and use of the data to the corresponding author via email. Source data are provided with this paper.

## Code availability

The custom codes in this study are upload to GitHub (<https://github.com/BGGDT/SCLIMS>). Codes are involved in further development of analytic methods in single-cell metabolomics. Therefore, the codes are under restricted access. The codes can be provided by the corresponding author upon requests explaining the aims and the use of the codes.

## References

- Cheng, S. et al. Single-Cell RNA-seq reveals cellular heterogeneity of pluripotency transition and X chromosome dynamics during early mouse development. *Cell Rep.* **26**, 2593–2607.e2593 (2019).
- Cao, J. et al. The single-cell transcriptional landscape of mammalian organogenesis. *Nature* **566**, 496–502 (2019).
- Magee, J. A., Piskounova, E. & Morrison, S. J. Cancer stem cells: impact, heterogeneity, and uncertainty. *Cancer Cell* **21**, 283–296 (2012).
- El-Sayes, N., Vito, A. & Mossman, K. Tumor heterogeneity: a great barrier in the age of cancer immunotherapy. *Cancers (Basel)* **13**, 806 (2021).
- Olbrecht, S. et al. High-grade serous tubo-ovarian cancer refined with single-cell RNA sequencing: specific cell subtypes influence survival and determine molecular subtype classification. *Genome Med.* **13**, 111 (2021).
- Kinker, G. S. et al. Pan-cancer single-cell RNA-seq identifies recurring programs of cellular heterogeneity. *Nat. Genet.* **52**, 1208–1218 (2020).
- Arrojo, E. D. R. et al. Age mosaicism across multiple scales in adult tissues. *Cell Metab.* **30**, 343–351.e343 (2019).
- Wang, S. et al. Single-cell transcriptomic atlas of primate ovarian aging. *Cell* **180**, 585–600.e519 (2020).
- Stoeckius, M. et al. Simultaneous epitope and transcriptome measurement in single cells. *Nat. Methods* **14**, 865–868 (2017).
- Peterson, V. M. et al. Multiplexed quantification of proteins and transcripts in single cells. *Nat. Biotechnol.* **35**, 936–939 (2017).
- Camunas-Soler, J. et al. Patch-Seq links single-cell transcriptomes to human islet dysfunction in diabetes. *Cell Metab.* **31**, 1017–1031.e1014 (2020).
- Lam, S. M. et al. A multi-omics investigation of the composition and function of extracellular vesicles along the temporal trajectory of COVID-19. *Nat. Metab.* **3**, 909–922 (2021).
- Lee, J. W. et al. Integrated analysis of plasma and single immune cells uncovers metabolic changes in individuals with COVID-19. *Nat. Biotechnol.* **40**, 110–120 (2022).
- Wilson, N. K. et al. Combined single-cell functional and gene expression analysis resolves heterogeneity within stem cell populations. *Cell Stem Cell* **16**, 712–724 (2015).
- Ghosh-Choudhary, S., Liu, J. & Finkel, T. Metabolic regulation of cell fate and function. *Trends Cell Biol.* **30**, 201–212 (2020).
- Lombard-Banek, C. et al. In vivo subcellular mass spectrometry enables proteo-metabolomic single-cell systems biology in a chordate embryo developing to a normally behaving tadpole (*X. laevis*). *Angew. Chem. Int. Ed.* **60**, 12852–12858 (2021).
- Zhu, H. et al. Single-neuron identification of chemical constituents, physiological changes, and metabolism using mass spectrometry. *Proc. Natl. Acad. Sci. USA* **114**, 2586–2591 (2017).
- Zhu, H. et al. Moderate UV exposure enhances learning and memory by promoting a novel glutamate biosynthetic pathway in the brain. *Cell* **173**, 1716–1727.e1717 (2018).
- Chang, X. et al. Methylated metabolites of chicoric acid ameliorate hydrogen peroxide (H<sub>2</sub>O<sub>2</sub>)-induced oxidative stress in HepG2 cells. *J. Agr. Food Chem.* **69**, 2179–2189 (2021).
- Bian, Y. Y. et al. Ferulic acid renders protection to HEK293 cells against oxidative damage and apoptosis induced by hydrogen peroxide. *Vitr. Cell Dev.* **51**, 722–729 (2015).
- Aguayo-Mazzucato, C. et al. Acceleration of beta cell aging determines diabetes and senolysis improves disease outcomes. *Cell Metab.* **30**, 129–142.e124 (2019).
- Chen, Q. & Ames, B. N. Senescence-like growth arrest induced by hydrogen peroxide in human diploid fibroblast F65 cells. *Proc. Natl. Acad. Sci. USA* **91**, 4130–4134 (1994).
- Hewitt, G. et al. Telomeres are favoured targets of a persistent DNA damage response in ageing and stress-induced senescence. *Nat. Commun.* **3**, 708 (2012).
- Jiang, D. et al. Post-GWAS functional analysis identifies CUX1 as a regulator of p16(INK4a) and cellular senescence. *Nat. Aging* **2**, 140–154 (2022).
- Aranda, A. et al. Dichloro-dihydro-fluorescein diacetate (DCFH-DA) assay: a quantitative method for oxidative stress assessment of nanoparticle-treated cells. *Toxicol. Vitr.* **27**, 954–963 (2013).
- McLennan, H. R. & Degli Esposti, M. The contribution of mitochondrial respiratory complexes to the production of reactive oxygen species. *J. Bioenerg. Biomembr.* **32**, 153–162 (2000).
- Aerts, J. T. et al. Patch clamp electrophysiology and capillary electrophoresis-mass spectrometry metabolomics for single cell characterization. *Anal. Chem.* **86**, 3203–3208 (2014).
- Yao, H. et al. Label-free mass cytometry for unveiling cellular metabolic heterogeneity. *Anal. Chem.* **91**, 9777–9783 (2019).
- Chakravarthi, S., Jessop, C. E. & Bulleid, N. J. The role of glutathione in disulphide bond formation and endoplasmic-reticulum-generated oxidative stress. *EMBO Rep.* **7**, 271–275 (2006).
- Ma, B., Guo, S., Nishina, Y. & Bianco, A. Reaction between graphene oxide and intracellular glutathione affects cell viability and proliferation. *ACS Appl. Mater. Interfaces* **13**, 3528–3535 (2021).
- Schomburg, D. & Schomburg, I. in *Springer Handbook of Enzymes: Class 1 · Oxidoreductases IX EC 1.6–1.8* (eds Schomburg, D. & Schomburg, I.) (Springer, 2005).
- Messina, S. A. & Dawson, R. Jr Attenuation of oxidative damage to DNA by taurine and taurine analogs. *Adv. Exp. Med. Biol.* **483**, 355–367 (2000).
- Dilberger, B. et al. Mitochondrial oxidative stress impairs energy metabolism and reduces stress resistance and longevity of *C. elegans*. *Oxid. Med. Cell. Longev.* **2019**, 6840540 (2019).
- Kalucka, J. et al. Quiescent endothelial cells upregulate fatty acid beta-oxidation for vasculoprotection via redox homeostasis. *Cell Metab.* **28**, 881–894.e813 (2018).
- Xia, J. & Wishart, D. S. MSEA: a web-based tool to identify biologically meaningful patterns in quantitative metabolomic data. *Nucleic Acids Res.* **38**, W71–W77 (2010).
- Liu, R. M. & Gaston Pravia, K. A. Oxidative stress and glutathione in TGF-beta-mediated fibrogenesis. *Free Radic. Biol. Med.* **48**, 1–15 (2010).
- Mytilineou, C., Kramer, B. C. & Yabut, J. A. Glutathione depletion and oxidative stress. *Parkinsonism Relat. Disord.* **8**, 385–387 (2002).



38. Chen, Z. et al. Oxidative stress and lipid dysregulation in lipid droplets: a connection to chronic kidney disease revealed in human kidney cells. *Antioxid. (Basel)* **11**, 1387 (2022).
39. Hu, C. et al. Oxidative stress-induced aberrant lipid metabolism is an important causal factor for dysfunction of immunocytes from patients with systemic lupus erythematosus. *Free Radic. Biol. Med.* **163**, 210–219 (2021).
40. Janero, D. R., Hreniuk, D. & Sharif, H. M. Hydrogen peroxide-induced oxidative stress to the mammalian heart-muscle cell (cardiomyocyte): nonperoxidative purine and pyrimidine nucleotide depletion. *J. Cell Physiol.* **155**, 494–504 (1993).
41. Liu, D., Ke, Z. & Luo, J. Thiamine deficiency and neurodegeneration: the interplay among oxidative stress, endoplasmic reticulum stress, and autophagy. *Mol. Neurobiol.* **54**, 5440–5448 (2017).
42. Ashoori, M. & Saedisomeolia, A. Riboflavin (vitamin B(2)) and oxidative stress: a review. *Br. J. Nutr.* **111**, 1985–1991 (2014).
43. Li, L. et al. Selecting representative samples from complex biological datasets using K-medoids clustering. *Front. Genet.* **13**, 954024 (2022).
44. Park, H. S. & Jun, C. H. A simple and fast algorithm for K-medoids clustering. *Expert Syst. Appl.* **36**, 3336–3341 (2009).
45. Aruoma, O. I., Halliwell, B., Hoey, B. M. & Butler, J. The antioxidant action of taurine, hypotaurine and their metabolic precursors. *Biochem. J.* **256**, 251–255 (1988).
46. Baliou, S. et al. Protective role of taurine against oxidative stress (Review). *Mol. Med. Rep.* **24**, 605 (2021).
47. Diez, V., Traikov, S., Schmeisser, K., Adhikari, A. K. D. & Kurzchalia, T. V. Glycolate combats massive oxidative stress by restoring redox potential in *Caenorhabditis elegans*. *Commun. Biol.* **4**, 151 (2021).
48. Zhang, F. et al. Characterization and heterologous expression of plasmalogen synthase MeHAD from *Megasphaera elsdenii*. *Biochim. Biophys. Acta Mol. Cell Biol. Lipids* **1868**, 159358 (2023).
49. Leist, A. K. et al. Mapping of machine learning approaches for description, prediction, and causal inference in the social and health sciences. *Sci. Adv.* **8**, eabk1942 (2022).
50. Rumelhart, D. E., Hinton, G. E. & Williams, R. J. Learning representations by back-propagating errors. *Nature* **323**, 533–536 (1986).
51. Goenawan, I. H., Bryan, K. & Lynn, D. J. DyNet: visualization and analysis of dynamic molecular interaction networks. *Bioinformatics* **32**, 2713–2715 (2016).
52. Huang, W., Hickson, L. J., Eirin, A., Kirkland, J. L. & Lerman, L. O. Cellular senescence: the good, the bad and the unknown. *Nat. Rev. Nephrol.* **18**, 611–627 (2022).
53. Cao, J. Y. et al. A genome-wide haploid genetic screen identifies regulators of glutathione abundance and ferroptosis sensitivity. *Cell Rep.* **26**, 1544–1556.e1548 (2019).
54. Toussaint, O., Medrano, E. E. & von Zglinicki, T. Cellular and molecular mechanisms of stress-induced premature senescence (SIPS) of human diploid fibroblasts and melanocytes. *Exp. Gerontol.* **35**, 927–945 (2000).
55. Hernandez-Segura, A., Nehme, J. & Demaria, M. Hallmarks of cellular senescence. *Trends Cell Biol.* **28**, 436–453 (2018).
56. Martin, G. M., Austad, S. N. & Johnson, T. E. Genetic analysis of ageing: role of oxidative damage and environmental stresses. *Nat. Genet.* **13**, 25–34 (1996).
57. Sharpless, N. E. & Sherr, C. J. Forging a signature of in vivo senescence. *Nat. Rev. Cancer* **15**, 397–408 (2015).
58. Chinopoulos, C., Tretter, L. & Adam-Vizi, V. Depolarization of in situ mitochondria due to hydrogen peroxide-induced oxidative stress in nerve terminals: inhibition of alpha-ketoglutarate dehydrogenase. *J. Neurochem.* **73**, 220–228 (1999).
59. Fang, X., Zhang, X. & Li, H. Oxidative stress and mitochondrial membrane potential are involved in the cytotoxicity of perfluorododecanoic acid to neurons. *Toxicol. Ind. Health* **36**, 892–897 (2020).
60. Friedman, D. B. & Johnson, T. E. A mutation in the age-1 gene in *Caenorhabditis elegans* lengthens life and reduces hermaphrodite fertility. *Genetics* **118**, 75–86 (1988).
61. Kenyon, C., Chang, J., Gensch, E., Rudner, A. & Tabtiang, R. A. *C. elegans* mutant that lives twice as long as wild type. *Nature* **366**, 461–464 (1993).
62. Liu, D., Zeng, X., Li, L. & Ou, Z. L. Carnitine promotes recovery from oxidative stress and extends lifespan in *C. elegans*. *Aging (Albany NY)* **13**, 813–830 (2020).
63. Janssens, G. E. et al. Transcriptomics-based screening identifies pharmacological inhibition of Hsp90 as a means to defer aging. *Cell Rep.* **27**, 467–480.e466 (2019).
64. Hsu, A. L., Feng, Z., Hsieh, M. Y. & Xu, X. Z. Identification by machine vision of the rate of motor activity decline as a lifespan predictor in *C. elegans*. *Neurobiol. Aging* **30**, 1498–1503 (2009).
65. Hernandez-Segura, A. et al. Unmasking transcriptional heterogeneity in senescent cells. *Curr. Biol.* **27**, 2652–2660.e2654 (2017).
66. Cohn, R. L., Gasek, N. S., Kuchel, G. A. & Xu, M. The heterogeneity of cellular senescence: insights at the single-cell level. *Trends Cell Biol.* **33**, 9–17 (2023).
67. Doha, Z. O. et al. MYC deregulation and PTEN loss model tumor and stromal heterogeneity of aggressive triple-negative breast cancer. *Nat. Commun.* **14**, 5665 (2023).
68. Aguayo-Mazzucato, C. et al. Beta cell aging markers have heterogeneous distribution and are induced by insulin resistance. *Cell Metab.* **25**, 898–910.e895 (2017).
69. Weng, C. et al. Single cell multiomic analysis reveals diabetes-associated beta-cell heterogeneity driven by HNF1A. *Nat. Commun.* **14**, 5400 (2023).
70. Garrido-Trigo, A. et al. Macrophage and neutrophil heterogeneity at single-cell spatial resolution in human inflammatory bowel disease. *Nat. Commun.* **14**, 4506 (2023).
71. Wu, C. Y. et al. Integrative single-cell analysis of allele-specific copy number alterations and chromatin accessibility in cancer. *Nat. Biotechnol.* **39**, 1259–1269 (2021).
72. Lake, B. B. et al. Integrative single-cell analysis of transcriptional and epigenetic states in the human adult brain. *Nat. Biotechnol.* **36**, 70–80 (2018).
73. Vicari, M. et al. Spatial multimodal analysis of transcriptomes and metabolomes in tissues. *Nat. Biotechnol.* **42**, 1046–1050 (2024).
74. Chen, S. et al. Integration of spatial and single-cell data across modalities with weakly linked features. *Nat. Biotechnol.* **42**, 1096–1106 (2024).
75. Singh, P. et al. Taurine deficiency as a driver of aging. *Science* **380**, eabn9257 (2023).
76. Candow, D. G. et al. Effectiveness of creatine supplementation on aging muscle and bone: focus on falls prevention and inflammation. *J. Clin. Med.* **8**, 488 (2019).
77. Smith, R. N., Agharkar, A. S. & Gonzales, E. B. A review of creatine supplementation in age-related diseases: more than a supplement for athletes. *F1000Res* **3**, 222 (2014).
78. Yoshida, R. et al. Metabolomics-based systematic prediction of yeast lifespan and its application for semi-rational screening of ageing-related mutants. *Aging Cell* **9**, 616–625 (2010).
79. Zhang, Y. et al. Glutamine suppresses senescence and promotes autophagy through glycolysis inhibition-mediated AMPKalpha lactylation in intervertebral disc degeneration. *Commun. Biol.* **7**, 325 (2024).
80. Kirov, I. I. et al. Global brain volume and N-acetyl-aspartate decline over seven decades of normal aging. *Neurobiol. Aging* **98**, 42–51 (2021).
81. Luo, T. et al. Asparagine prevents intestinal stem cell aging via the autophagy-lysosomal pathway. *Aging Cell* e14423 (2024).
82. Huh, D. & Paulsson, J. Random partitioning of molecules at cell division. *Proc. Natl Acad. Sci. USA* **108**, 15004–15009 (2011).

83. Knoblich, J. A. Asymmetric cell division: recent developments and their implications for tumour biology. *Nat. Rev. Mol. Cell Biol.* **11**, 849–860 (2010).
  84. Sunchu, B. & Cabernard, C. Principles and mechanisms of asymmetric cell division. *Development* **147**, dev167650 (2020).
  85. Griffin, E. E. Cytoplasmic localization and asymmetric division in the early embryo of *Caenorhabditis elegans*. *Wires Dev. Biol.* **4**, 267–282 (2015).
  86. Correia-Melo, C. et al. Cell-cell metabolite exchange creates a pro-survival metabolic environment that extends lifespan. *Cell* **186**, 63–79 e21 (2023).
  87. Martinez-Cue, C. & Rueda, N. Cellular senescence in neurodegenerative diseases. *Front. Cell Neurosci.* **14**, 16 (2020).
  88. Martini, H. et al. Selective cardiomyocyte oxidative stress leads to bystander senescence of cardiac stromal cells. *Int J. Mol. Sci.* **22**, 2245 (2021).
  89. Guimaraes-Ferreira, L. Role of the phosphocreatine system on energetic homeostasis in skeletal and cardiac muscles. *Einstein (Sao Paulo)* **12**, 126–131 (2014).
  90. Fontana, D. et al. ETNK1 mutations induce a mutator phenotype that can be reverted with phosphoethanolamine. *Nat. Commun.* **11**, 5938 (2020).
  91. El-Bacha, T. & Torres, A. G. in *Encyclopedia of Food and Health* (eds Caballero, B., Finglas, P. M. & Toldrá, F) (Academic Press, 2016).
  92. Zenin, A. et al. Identification of 12 genetic loci associated with human healthspan. *Commun. Biol.* **2**, 41 (2019).
  93. Partridge, L., Fuentealba, M. & Kennedy, B. K. The quest to slow ageing through drug discovery. *Nat. Rev. Drug Discov.* **19**, 513–532 (2020).
  94. Zhou, Z. et al. Ion mobility collision cross-section atlas for known and unknown metabolite annotation in untargeted metabolomics. *Nat. Commun.* **11**, 4334 (2020).
  95. Bouwmeester, R. et al. Predicting ion mobility collision cross sections and assessing prediction variation by combining conventional and data driven modeling. *Talanta* **274**, 125970 (2024).
  96. Baker, E. S. et al. METLIN-CCS: an ion mobility spectrometry collision cross section database. *Nat. Methods* **20**, 1836–1837 (2023).
  97. Habe, T. T. et al. Ultrahigh-throughput ESI-MS: sampling pushed to six samples per second by acoustic ejection mass spectrometry. *Anal. Chem.* **92**, 12242–12249 (2020).
  98. Grienberger, C. & Konnerth, A. Imaging calcium in neurons. *Neuron* **73**, 862–885 (2012).
  99. Eastman, A. E. et al. Resolving cell cycle speed in one snapshot with a live-cell fluorescent reporter. *Cell Rep.* **31**, 107804 (2020).
- YD9100002005 to H.Z.), Research Funds of Center for Advanced Interdisciplinary Science and Biomedicine of IHM (QYD20230011 to W.X.), CAS Project for Young Scientists in Basic Research (YSBR-013 to W.X.), Anhui Provincial Major Science and Technology Project (Grant 202303a07020005 to W.X.), University Synergy Innovation Program of Anhui Province (Grant number GXXT-2022-033 to H.Z.).

## Author contributions

W.X. initialized, designed, and supervised the study with the assistance of H.Z. Z.W. conducted single-cell sampling, cellular and *C. elegans* experiments. S. G. conducted single-cell sampling of MEFs. Z.W. and H.Z. conducted SCMS analysis. Z.W. analyzed the metabolomic data. M.Y., T.L., and W. L. processed the raw metabolomic data. M.Y. conducted the pseudotime analysis. Z.W. performed the experiments of cellular senescence rescue of metabolites with the assistance of W.Q. Q. C. assisted in culture of MEFs. X. C. assisted in the selection and design of GSH probe. Q. Z. assisted in the analysis related to mitochondria and *C. elegans*. Z. J. assisted in the analysis related to cellular senescence. Z.W. wrote the manuscript. W.X. and H.Z. led the discussion, reviewed and edited the manuscript.

## Competing interests

The authors declare no competing interests.

## Additional information

**Supplementary information** The online version contains supplementary material available at <https://doi.org/10.1038/s41467-025-57992-3>.

**Correspondence** and requests for materials should be addressed to Hongying Zhu or Wei Xiong.

**Peer review information** *Nature Communications* thanks Christopher Anderton, Kiryl Piatkevich and Zhiwei Zhou for their contribution to the peer review of this work. A peer review file is available.

**Reprints and permissions information** is available at <http://www.nature.com/reprints>

**Publisher's note** Springer Nature remains neutral with regard to jurisdictional claims in published maps and institutional affiliations.

**Open Access** This article is licensed under a Creative Commons Attribution-NonCommercial-NoDerivatives 4.0 International License, which permits any non-commercial use, sharing, distribution and reproduction in any medium or format, as long as you give appropriate credit to the original author(s) and the source, provide a link to the Creative Commons licence, and indicate if you modified the licensed material. You do not have permission under this licence to share adapted material derived from this article or parts of it. The images or other third party material in this article are included in the article's Creative Commons licence, unless indicated otherwise in a credit line to the material. If material is not included in the article's Creative Commons licence and your intended use is not permitted by statutory regulation or exceeds the permitted use, you will need to obtain permission directly from the copyright holder. To view a copy of this licence, visit <http://creativecommons.org/licenses/by-nc-nd/4.0/>.

© The Author(s) 2025

## Acknowledgements

The authors thank Professor Quan Wen (University of Science and Technology of China) for providing the N2 *C. elegans* strain. We thank Professor Chunlei Cang (University of Science and Technology of China) for providing MEFs. This study was supported by National Key R&D Program of China (2021YFA0804900, 2020YFA0112203), National Natural Science Foundation of China (Grants 32225020, 32430045, 92049304, 32121002 to W.X., 32322033, 32471080, 21974130 and 91849116 to H.Z.), the Strategic Priority Research Program of the Chinese Academy of Sciences (Grant XDB39050000 to W.X.), Key Research Program of Frontier Science (CAS, Grant No. ZDBS-LY-SM002 to W.X.), CAS Interdisciplinary Innovation Team (JCTD-2018-20 to W.X.), the Youth Innovation Promotion Association CAS, the Fundamental Research Funds for the Central Universities, USTC Research Funds of the Double First-Class Initiative (YD9100002001 to W.X. and